Thermocapillary migration of interfacial droplets

Edwin F. Greco and Roman O. Grigoriev
Center for Nonlinear Science and School of Physics, Georgia Institute of Technology, Atlanta, Georgia 30332-0430, USA

(Received 31 August 2008; accepted 2 February 2009; published online 16 April 2009)

We study the thermocapillary driven motion of a droplet suspended at an interface of two fluid layers subjected to an imposed temperature gradient parallel to the interface. We compute the temperature and velocity fields inside and outside of the droplet using a boundary collocation numerical scheme in the limit of small capillary and thermal Péclet numbers and compare the results with the classical problem of thermocapillary migration of a droplet in the bulk. In particular, we find that, for typical values of parameters, interfacial droplets migrate in the direction opposite to the temperature gradient, while in the classical problem migration is always in the direction of the gradient. Furthermore, we find that a rich variety of flow structures can emerge inside interfacial droplets. We also confirm that for parameters matching a recent experimental study of mixing inside interfacial microdroplets [R. O. Grigoriev, V. Sharma, and M. F. Schatz, Lab Chip **6**, 1369 (2006)] the interior flow can be approximated with reasonable accuracy by assuming the droplet to be completely submerged in the bottom layer. © *2009 American Institute of Physics*.
[DOI: 10.1063/1.3112777]

I. INTRODUCTION

The first published investigation of thermocapillary migration dates back almost 50 years to the work by Young *et al.*,[1] who observed and analyzed the motion of air bubbles in silicon oil in response to the imposed temperature gradient. The migration velocity was found to depend linearly on both the bubble radius and the temperature gradient. It was also demonstrated that by aligning the temperature gradient with gravity, the migration of the bubbles could be arrested or even reversed. In addition to these observations, a steady-state analytical solution was computed for the velocity field and migration velocity in the limit of small Reynolds, capillary, and thermal Péclet numbers. This solution was found to be in good agreement with the experimental observations of a gas bubble. The analytical result was later shown, experimentally, to also accurately describe the thermocapillary migration of immiscible liquid droplets.[2]

More recent studies have concentrated on the experimental verification of the predicted migration velocity for a droplet in a low gravity environment,[3–8] where thermocapillary migration becomes a more efficient mechanism for removing bubbles from liquids due to the weakness of buoyancy. Changes in the migration velocity due to neighboring bubbles or drops[9–12] and solid or free boundaries[13–17] have also been extensively studied. For a comprehensive review of these topics, the interested reader is referred to the excellent book by Subramanian and Balasubramanian.[18]

The current interest in the dynamics of *interfacial* droplets is primarily driven by applications to digital microfluidic devices, such as the one investigated by Grigoriev *et al.*,[19] who demonstrated experimentally that thermal gradients could be used for both transport and mixing inside droplets suspended on an immiscible liquid substrate and ranging from millimeters to microns in size. Detailing the dynamics of interfacial droplets, subjected to an external temperature gradient, is considerably more complicated. First, the shape of interfacial droplets is generally not spherical and must be determined using the surface tensions at three different interfaces. Second, the presence of a contact line (i.e., the line where the three fluids contact each other) both affects the total force on the droplet and places additional constraints on the velocity field. Last, but certainly not least, the problem is further complicated by the fact that an interfacial droplet is in contact with not one, but *two* exterior fluids with different physical properties (surface tension, viscosity, etc.), so that the usual top-bottom symmetry of the solution is broken.

All these factors have likely contributed to a much more limited understanding of the dynamics of interfacial droplets, regardless of the physical mechanism driving the flow. To our knowledge, there are very few published results concerning the motion of interfacial drops in the presence of a temperature gradient. Besides the previously mentioned study by Grigoriev *et al.*,[19] Rybalko *et al.*[20] investigated experimentally the motion of an interfacial droplet directly heated with a laser beam. A coarse image of the velocity field inside the droplet was reconstructed using particle-image velocimetry, and the velocity of thermocapillary migration was measured as a function of the laser power. The direction of the droplet motion was shown to reverse when the heating was switched from the top of the droplet to the bottom.

The dynamics of, and mixing inside, thermocapillary driven interfacial droplets was investigated theoretically by Grigoriev[21] for a time-dependent thermal gradient and more recently by Vainchtein *et al.*[22] for a time-independent thermal gradient. Both of these studies considered a highly simplified model (based on Lamb's general solution[23]) of a spherical droplet completely submerged in the substrate fluid and the theoretical results were found to be in qualitative agreement with the experimental observations.

We should also note two other studies which investigated the flows in interfacial droplets driven by mechanisms other than thermocapillarity. Smith *et al.*[24] numerically computed the flow inside a two-dimensional (2D) interfacial drop subjected to an imposed simple shear flow in the substrate fluid. They discovered that the interior flow pattern inside the droplet was topologically similar to that of a spherical droplet in an unbounded sheared fluid.[25] In addition, the droplet was observed to pinch off from the confining interface for large shear rates. Craster and Matar[26] investigated the shape dynamics of a droplet spreading out over the supporting interface due to the action of surface tension forces. Their analysis of slender droplets used the lubrication approximation to derive a set of differential equations for the time evolution of the droplet shape.

While a relatively crude model might be sufficient for describing the overall motion of an interfacial droplet, a quantitative description of mixing requires an accurate knowledge of the flow field inside the droplet. Even though approximate analytical methods can provide valuable insights in certain limiting cases (e.g., lubrication analysis for very slender droplets or Lamb's expansion for nearly spherical drops), the solution for a general case can only be obtained numerically. Our goal in this paper, therefore, will be to obtain such numerical solutions for the flow field inside and outside the interfacial droplet subjected to an imposed temperature gradient in the substrate. The exterior solution will determine the thermocapillary migration speed relative to the bottom of the substrate. Computing the interior flow will allow us to quantify mixing inside the droplet and, in particular, gauge the accuracy of the simplified model.[21]

We begin in Sec. II by introducing the governing equations. The numerical boundary collocation scheme used to obtain the solution is described in Sec. III. The results are summarized in Sec. IV. Finally, Sec. V contains our conclusions.

II. PROBLEM DESCRIPTION

Consider a droplet (fluid 3) suspended at the interface $\partial\Omega_{12}$ between a substrate fluid (fluid 2) and a covering fluid (fluid 1), as illustrated in Fig. 1. The substrate layer of thickness H and width L is supported by a flat horizontal solid surface below, while the covering fluid is assumed to be unbounded above. The droplet is bounded above by the interface $\partial\Omega_{13}$ with the covering fluid and below by the interface $\partial\Omega_{23}$ with the substrate fluid. The origin for the coordinate system is chosen, unless specified otherwise, at the center of mass of the droplet.

A. Governing equations

Since this work is mainly motivated by its applications to microfluidics, we will assume the velocities to be small enough for convective momentum and energy transport to be negligible and ignore gravity. We will also restrict our attention to the steady flows. In the limit of the vanishing Reynolds number, Re=0, the velocity fields in all three fluids are governed by the Stokes equation subject to the incompressibility condition

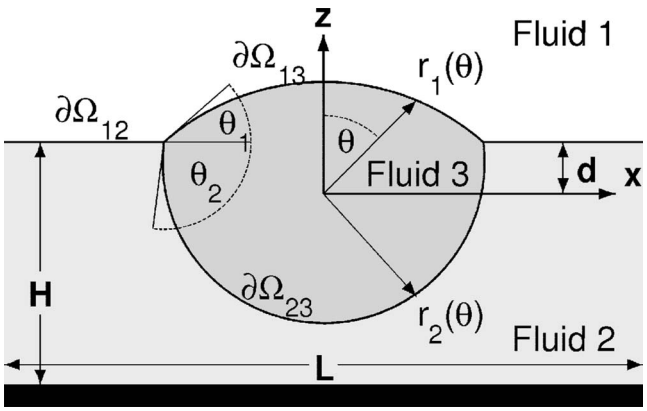

FIG. 1. A view of the interfacial drop in the (x,z) plane (not to scale). We take the z axis to be vertical and the x axis to point in the direction of the imposed temperature gradient. The droplet is symmetric with respect to rotation about the z axis (see Sec. II D).

$$\nabla \cdot \mathbf{V}_i = 0, \tag{1a}$$

$$\mu_i \nabla^2 \mathbf{V}_i = \nabla p_i, \tag{1b}$$

where μ_i is the dynamic viscosity of fluid i, $\mathbf{V}_i$, and p_i are the corresponding velocity and pressure. In the limit of vanishing thermal Péclet number, Pe=0, the temperature field in each fluid must satisfy the Laplace equation

$$\nabla^2 T_i = 0. \tag{2}$$

The boundary conditions for the temperature field at a fluid-fluid interface $\partial\Omega_{ij}$ require the continuity of the temperature field and the heat flux

$$(T_j - T_i)|_{\partial\Omega_{ij}} = 0, \tag{3a}$$

$$(k_j \nabla T_j - k_i \nabla T_i) \cdot \hat{\mathbf{n}}|_{\partial\Omega_{ij}} = 0, \tag{3b}$$

where k_i is the thermal conductivity of fluid i and the normal vector $\hat{\mathbf{n}}$ points from fluid i into fluid j. Furthermore, at $\partial\Omega_{ij}$ the normal component of the velocity must vanish and the tangential component of the velocity must be continuous

$$\mathbf{V}_j \cdot \hat{\mathbf{n}}|_{\partial\Omega_{ij}} = \mathbf{V}_i \cdot \hat{\mathbf{n}}|_{\partial\Omega_{ij}} = 0, \tag{4a}$$

$$(\mathbf{V}_j - \mathbf{V}_i) \times \hat{\mathbf{n}}|_{\partial\Omega_{ij}} = \mathbf{0}, \tag{4b}$$

where the position of the interface is assumed stationary. Finally, the jump in the tangential and normal components of the stress tensor Σ must balance the surface tension stresses at the interface

$$\hat{\mathbf{n}} \times (\Sigma_j - \Sigma_i) \cdot \hat{\mathbf{n}}|_{\partial\Omega_{ij}} = -(\hat{\mathbf{n}} \times \nabla)\sigma_{ij}, \tag{5a}$$

$$\hat{\mathbf{n}} \cdot (\Sigma_j - \Sigma_i) \cdot \hat{\mathbf{n}}|_{\partial\Omega_{ij}} = \sigma_{ij} \nabla \cdot \hat{\mathbf{n}}. \tag{5b}$$

All physical properties of the fluids, excluding surface tension, are assumed to be independent of temperature. Surface tension is assumed to vary linearly with temperature

$$\sigma_{ij}(T) = \bar{\sigma}_{ij} + \sigma'_{ij}(T - T_0), \tag{6}$$

where $\bar{\sigma}_{ij}$ is the value of the surface tension at the interface between fluids i and j at the reference temperature T_0 (defined as the temperature at the origin) and σ'_{ij} is the corresponding temperature coefficient.

Since we are interested in small droplets, it is safe to assume the temperature variation to be small near the droplet (where the curvature $\nabla \cdot \hat{\mathbf{n}}$ is large), so that we can rewrite the stress boundary conditions (5) as

$$\hat{\mathbf{n}} \times (\Sigma_j - \Sigma_i) \cdot \hat{\mathbf{n}}|_{\partial\Omega_{ij}} = -\sigma'_{ij}\hat{\mathbf{n}} \times \nabla T_i, \tag{7a}$$

$$\hat{\mathbf{n}} \cdot (\Sigma_j - \Sigma_i) \cdot \hat{\mathbf{n}}|_{\partial\Omega_{ij}} = \bar{\sigma}_{ij} \nabla \cdot \hat{\mathbf{n}}. \tag{7b}$$

B. External flow and temperature fields far from the droplet

Additional boundary conditions for fluids 1 and 2 should be satisfied far from the droplet (e.g., at the sidewalls, top, and bottom of the container). To get an analytically tractable solution, we will assume that the temperature gradient is generated by maintaining the sidewalls of the container at different, fixed temperatures

$$T|_{x=-L/2} = T_l, \quad T|_{x=L/2} = T_r. \tag{8}$$

The vertical component of the heat flux at the top and bottom of the container is assumed negligible,

$$\partial_z T|_{z=d-H} = \partial_z T|_{z\to\infty} = 0, \tag{9}$$

where, without loss of generality, we chose to place the origin symmetrically between the side walls, a distance $H-d$ above the bottom of the container. Furthermore, a no-slip boundary condition is assumed at the bottom of the container

$$\mathbf{V}|_{z=d-H} = \mathbf{0} \tag{10}$$

and a stress-free, no-flux boundary condition is assumed at the top

$$V_z|_{z\to\infty} = 0, \quad (\partial_z V_x + \partial_x V_z)|_{z\to\infty} = 0. \tag{11}$$

The extent of the fluids in the y-direction (out of the page in Fig. 1) is taken to be sufficiently large, such that far from the droplet the flow can be considered 2D. Furthermore, the thickness H of the substrate layer is taken to be much smaller than its width L and the temperature of the right sidewall T_r is assumed greater than the temperature of the left sidewall T_l. The difference in temperatures of the two sidewalls is assumed sufficiently small to allow the temperature and velocity fields in the substrate to reach a steady state. Finally, the droplet is assumed to be sufficiently small, so its presence does not significantly affect the temperature and velocity in the fluids far away.

Under these conditions, in the limit of the vanishing droplet size (such that the interface $\partial\Omega_{12}$ coincides with the plane $z=d$), the steady-state solution for the temperature and velocity fields in the substrate and the covering fluid can be computed using perturbation theory, where the small parameter is the aspect ratio H/L, following Levich[27] and Subramanian and Balasubramanian.[18] Using our notations, the temperature and velocity fields are

$$T_1^\infty = T_2^\infty = T_0 + \Theta x, \tag{12a}$$

$$\mathbf{V}_1^\infty = \frac{\sigma'_{12} H \Theta}{4\mu_2}\hat{\mathbf{x}}, \tag{12b}$$

$$\mathbf{V}_2^\infty = \frac{\sigma'_{12}\Theta}{\mu_2}\left(\frac{3}{4H}(z-d)^2 + z - d + \frac{H}{4}\right)\hat{\mathbf{x}}, \tag{12c}$$

where the superscript is used to designate these fields as asymptotic, and

$$\Theta \equiv \frac{T_r - T_l}{L}. \tag{13}$$

The characteristic length scale on which the surface tension $\sigma_{12}[T(x)]$ varies is given by

$$l_0 \equiv \frac{\bar{\sigma}_{12}}{|\sigma'_{12}|\Theta}, \tag{14}$$

where the absolute value reflects the fact that typically $\sigma'_{ij} < 0$. Strictly speaking, linear approximation (6), and hence solution (12), is only valid at length scales of order l_0 or smaller. The introduction of a droplet of characteristic size r_0 small compared to both this length scale and the depth of the substrate H will distort solution (12) only near the droplet, while far from the droplet (i.e., for $r_0 \ll |\mathbf{x}| \lesssim l_0$) we can expect it to remain accurate. Similarly, the substrate's free surface $\partial\Omega_{12}$ will generally be curved near the droplet and approach the horizontal plane $z=d$ far from the droplet. Finally, although solution (12) does not satisfy a no-slip boundary condition at the side walls, the region where it is inaccurate only extends an $O(H)$ distance from the sidewalls.

In the following it will be convenient to choose the reference frame in which the droplet is stationary. The symmetry of the problem implies that the droplet moves along the x axis. Switching to a reference frame moving with velocity $\mathbf{U_0} = U_0\hat{\mathbf{x}}$, the following asymptotic boundary conditions on the velocity and temperature fields are obtained:

$$\mathbf{V}_i \to \mathbf{V}_i^\infty - \mathbf{U_0}, \quad |\mathbf{x}| \to \infty, \tag{15a}$$

$$T_i \to T_i^\infty, \quad |\mathbf{x}| \to \infty, \tag{15b}$$

for $i=1,2$. In this reference frame all fluid-fluid interfaces $\partial\Omega_i$ are stationary and boundary condition (4) applies.

C. Nondimensional parameters

Solution (12) is valid in the limit of small Reynolds and thermal Péclet numbers. There are, however, several different length and velocity scales in this problem. For the flow far from the droplet the characteristic scales are $l_1 = l_2 = H$ and $v_1 = v_2 = V_1^\infty$. Near the droplet the scales are $l_3 = r_0$ and $v_3 = v_0$, where

$$v_0 \equiv \frac{|\sigma'_{23}| r_0}{\mu_2} \Theta \tag{16}$$

is the characteristic velocity of thermocapillary driven flow inside the droplet. Using these scales we can define the Reynolds numbers

$$\mathrm{Re}_i \equiv \frac{l_i v_i \rho_i}{\mu_i} \tag{17}$$

and the thermal Péclet numbers

$$\mathrm{Pe}_i \equiv \frac{l_i v_i \rho_i C_{p,i}}{k_i}, \tag{18}$$

for each of the three fluids, using the respective values of the densities ρ_i, viscosities μ_i, thermal conductivities k_i, and heat capacities $C_{p,i}$.

The differences in the length and velocity scales mean that the Reynolds and Péclet numbers for different fluids can differ by orders of magnitude. For instance, even assuming all the material parameters are comparable, we find

$$\frac{\mathrm{Re}_2}{\mathrm{Re}_3} = \frac{1}{4} \frac{\rho_2}{\rho_3} \frac{\mu_3}{\mu_2} \frac{|\sigma'_{12}|}{|\sigma'_{23}|} \frac{H^2}{r_0^2} \sim \frac{H^2}{r_0^2}, \tag{19}$$

a ratio exceeding 100 in experiments.[19] However, both v_0 and V_1^∞, and with them Re_i and Pe_i for each fluid, can be made arbitrarily small by reducing the imposed temperature gradient Θ.

In addition to the Reynolds and Péclet numbers, it will be convenient to introduce the capillary and Bond numbers. In particular, the capillary numbers can be defined for each fluid as

$$\mathrm{Ca}_i = \frac{\mu_i v_0}{\bar{\sigma}_i}, \quad \bar{\sigma}_i = \begin{cases} \bar{\sigma}_{i3}, & i = 1,2, \\ \bar{\sigma}_{23}, & i = 3, \end{cases} \tag{20}$$

and are all of the same order of magnitude in the typical case when the surface tensions and viscosities of all three fluids are comparable. The condition of the smallness of the capillary numbers is equivalent to the condition $l_0 \gg r_0$. For instance, for the substrate fluid we have

$$\mathrm{Ca}_2 \equiv \frac{\mu_2 v_0}{\bar{\sigma}_{23}} = \frac{|\sigma'_{23}|}{|\sigma'_{12}|} \frac{\bar{\sigma}_{12}}{\bar{\sigma}_{23}} \frac{r_0}{l_0} \sim \frac{r_0}{l_0}. \tag{21}$$

The Bond numbers are defined as

$$\mathrm{Bo}_i \equiv \frac{\rho_i g r_0^2}{\bar{\sigma}_i}, \tag{22}$$

where g is the gravitational acceleration and $\bar{\sigma}_i$ is defined in Eq. (20). The three Bond numbers are, again, all of the same order of magnitude for fluids with comparable densities and surface tensions. For typical fluids they quickly become very small as the droplet size decreases (e.g., one finds $\mathrm{Bo} \sim 0.1$ already for a 1 mm water droplet). We, therefore, restrict our attention to the limit of small Bond numbers, where the effects of gravity can be ignored.

To reduce the number of parameters describing the problem to a minimum, we nondimensionalize our governing equations and boundary conditions by rescaling all dimensional variables. We scale all lengths by r_0. Temperature is scaled by first subtracting T_0 and then dividing by the characteristic temperature scale Θr_0. All velocities are scaled by the characteristic velocity v_0. All stresses, including pressure, are scaled by the typical viscous stress $\Sigma_0 = |\sigma'_{23}|\Theta$. The viscosities, thermal conductivities, reference surface tensions, and temperature coefficients of surface tension are scaled by μ_2, k_2, $\bar{\sigma}_{23}$, and σ'_{23}, respectively. The corresponding nondimensional quantities are summarized in Table I. In addition to these eight $O(1)$ parameters we find two large parameters, the nondimensional temperature length scale $\lambda = l_0/r_0$ and substrate depth $\chi = H/r_0$.

TABLE I. Dimensionless parameters describing thermocapillary migration of an interfacial droplet.

	Fluid 1	Fluid 2	Fluid 3
Viscosity	$\alpha_1 = \frac{\mu_1}{\mu_2}$	$\alpha_2 = 1$	$\alpha_3 = \frac{\mu_3}{\mu_2}$
Thermal conductivity	$\beta_1 = \frac{k_1}{k_2}$	$\beta_2 = 1$	$\beta_3 = \frac{k_3}{k_2}$
Surface tension	$\gamma_{12} = \frac{\bar{\sigma}_{12}}{\bar{\sigma}_{23}}$	$\gamma_{13} = \frac{\bar{\sigma}_{13}}{\bar{\sigma}_{23}}$	$\gamma_{23} = 1$
Temperature coefficient	$\tau_{12} = \frac{\sigma'_{12}}{\sigma'_{23}}$	$\tau_{13} = \frac{\sigma'_{13}}{\sigma'_{23}}$	$\tau_{23} = 1$

D. Droplet shape

The shape of the free interfaces determining both the droplet shape and the shape of the surface of the substrate fluid which is generally deformed by the droplet, are found by solving the normal stress balance equation (7b). In the limit $\mathrm{Bo} = \mathrm{Ca} = 0$ considered here, the normal component of the stress reduces to a constant pressure. Consequently, all three interfaces are surfaces of constant curvature. Since $\partial\Omega_{12}$ is flat far from the droplet, it has to coincide with the horizontal flat plane $z = d$ everywhere. Similarly, the top and bottom surfaces of the droplet, $\partial\Omega_{13}$ and $\partial\Omega_{23}$, will be spherical caps of constant curvature.

We define θ_1 and θ_2 to be the contact angles that the interfaces $\partial\Omega_{13}$ and $\partial\Omega_{23}$, respectively, make with $\partial\Omega_{12}$ (see Fig. 1). These angles can be determined from a simple force balance at the contact line

$$\bar{\sigma}_{12} = \bar{\sigma}_{13} \cos\theta_1 + \bar{\sigma}_{23} \cos\theta_2, \tag{23a}$$

$$0 = \bar{\sigma}_{13} \sin\theta_1 - \bar{\sigma}_{23} \sin\theta_2. \tag{23b}$$

The radii of curvature, R_1 and R_2, of the top and bottom caps of the interfacial drop, are determined by solving the Young–Laplace equation obtained from Eq. (7b)

$$\frac{\bar{\sigma}_{13}}{\bar{\sigma}_{23}} = \frac{R_1}{R_2}, \tag{24}$$

subject to the condition that the droplet volume is equal to that of a sphere with radius r_0

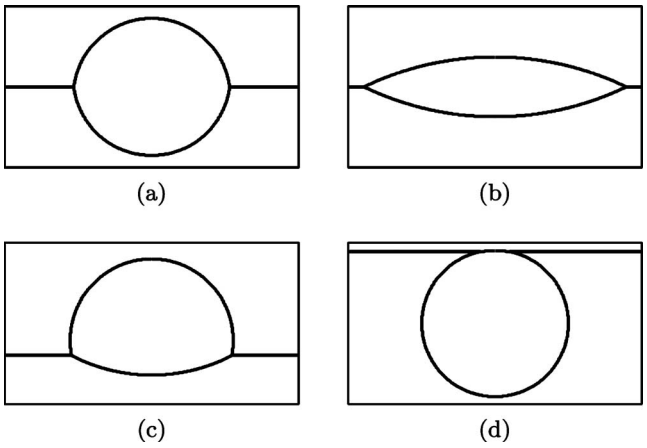

FIG. 2. Interfacial droplet shape dependence on surface tensions. A $y=0$ cross section is shown for (a) $\gamma_{12}=0.25$ and $\gamma_{13}=1$, (b) $\gamma_{12}=1.8$ and $\gamma_{13}=1$, (c) $\gamma_{12}=0.80$ and $\gamma_{13}=0.47$, and (d) $\gamma_{12}=1$ and $\gamma_{13}=2$.

$$4r_0^3 = R_1^3(2-3\cos\theta_1+\cos^3\theta_1) + R_2^3(2-3\cos\theta_2+\cos^3\theta_2). \tag{25}$$

With the origin of the coordinate system placed at the droplet's center of mass we find the submersion length

$$d = \frac{1}{16r_0^3}[R_1^4(\cos\theta_1+3)(\cos\theta_1-1)^3 - R_2^4(\cos\theta_2+3)(\cos\theta_2-1)^3]. \tag{26}$$

All three interfaces possess axial symmetry with respect to the z axis, so in spherical polar coordinates, the top cap $\partial\Omega_{13}$ can be parameterized as

$$r_1(\theta) = -h_1\cos\theta + \sqrt{R_1^2 - h_1^2\sin^2\theta}, \tag{27a}$$

$$h_1 \equiv R_1\cos\theta_1 - d, \tag{27b}$$

and the bottom cap $\partial\Omega_{23}$ as

$$r_2(\theta) = -h_2\cos\theta + \sqrt{R_2^2 - h_2^2\sin^2\theta}, \tag{28a}$$

$$h_2 \equiv -R_2\cos\theta_2 - d. \tag{28b}$$

We should note that, for certain values of parameters, it may be more convenient to place the origin in the plane of the interface $\partial\Omega_{12}$, i.e., set $d=0$.

The contact line Γ_c, defined as the intersection of the hemispheres $\partial\Omega_{13}$ and $\partial\Omega_{23}$, is a circle with polar coordinates $r=r_c$ and $\theta=\theta_c$ such that $r_c=r_1(\theta_c)=r_2(\theta_c)$. Alternatively, Γ_c can be described as a circle of radius $r_c\sin\theta_c$ that lies in the plane $z=d=r_c\cos\theta_c$.

One of the important differences between interfacial and fully submerged droplets is that the latter are spherical (in the limit Bo=Ca=0) while the former are generally not. Some representative examples of interfacial droplet shapes are shown in Fig. 2. As the force balance conditions (27) and (28) show, the interfacial droplet can be spherical only in the limit of vanishing nondimensional surface tension γ_{12} at the substrate surface. As γ_{12} increases from zero, the width-to-height aspect ratio of the droplet also increases, with the droplet stretched by the surface tension at $\partial\Omega_{12}$ [compare Figs. 2(a) and 2(b)]. There is no steady-state solution for the droplet shape for $\gamma_{12}>1+\gamma_{13}$; over time the droplet becomes thinner and thinner. In this limit, at long times, the solution is well described by the lubrication approximation.[26]

The nondimensional surface tension γ_{13} at the upper surface of the droplet controls the degree of submersion of the droplet. Interfacial droplets in steady-state will exist for $|1-\gamma_{12}|<\gamma_{13}<1+\gamma_{12}$, with $\gamma_{13}=1$ corresponding to the droplet being symmetric with respect to the substrate surface [see Fig. 2(b)]. Decreasing γ_{13} below unity forces the droplet to be expelled by the substrate fluid [see Fig. 2(c)], while increasing γ_{13} above unity increases the submersion of the droplet into the substrate fluid, with $\gamma_{13}=1+\gamma_{12}$ corresponding to complete encapsulation [see Fig. 2(d)] and $\gamma_{13}=|1-\gamma_{12}|$—complete expulsion. (In these two limits the droplet also becomes spherical.)

E. Thermocapillary migration speed

Our assumption that the droplet is stationary in the chosen reference frame requires that the total force on the droplet vanish

$$\mathbf{f} = \mathbf{f}_{\text{body}} + \mathbf{f}_{\text{surface}} + \mathbf{f}_{\text{line}} = \mathbf{0}. \tag{29}$$

In the Bo=0 limit the body force $\mathbf{f}_{\text{body}}$ is absent. The surface force is given by

$$\mathbf{f}_{\text{surface}} = \int_{\partial\Omega_{13}} \Sigma_1\cdot\mathbf{n}\,dS + \int_{\partial\Omega_{23}} \Sigma_2\cdot\mathbf{n}\,dS. \tag{30}$$

The line force exerted on the droplet by the surface tension at the interface $\partial\Omega_{12}$,

$$\mathbf{f}_{\text{line}} = \int_{\Gamma_c} \sigma_{12}d\mathbf{s}\times\hat{\mathbf{z}}, \tag{31}$$

does not vanish due to the variation in the surface tension along the contact line. Because the surface tension is larger where the fluid is cooler, the contact line force pulls the drop in the direction opposite to that of the imposed temperature gradient.

The contour integral (31) can be evaluated by writing $d\mathbf{s}=r_c\sin\theta_c d\phi\hat{\phi}$, where $\hat{\phi}$ is the unit vector corresponding to the azimuthal angle ϕ of the spherical polar coordinate system (r,θ,ϕ). Using Eq. (6) we find

$$\mathbf{f}_{\text{line}} = \sigma'_{12}r_c\sin\theta_c\hat{\mathbf{x}}\int_0^{2\pi} T\cos\phi d\phi. \tag{32}$$

The force constraint (29) closes our system of equations for the velocity fields, allowing the computation of the speed $\mathbf{U_0}$ of the droplet relative to the bottom of the substrate fluid layer.

III. NUMERICAL METHOD

A. Temperature and velocity fields

The temperature and velocity fields in each fluid can be found by solving Eqs. (1) and (2) subject to the boundary conditions stated previously. The general solution for the temperature field can be expressed in terms of spherical har-

monics. The interior temperature must be bounded at the origin and the exterior temperature must satisfy Eq. (15b) far from the droplet. The temperature field must also be symmetric in y and antisymmetric in x. Since both the Laplace equation (2) and the boundary conditions (3) are linear, these constraints yield the following general solution for the nondimensional temperature field:

$$T_i = r\sin\theta\cos\phi + \sum_{n=1}^{\infty} D_i^n \frac{1}{r^{n+1}} P_n^1(\cos\theta)\cos\phi, \quad i=1,2, \tag{33a}$$

$$T_3 = \sum_{n=1}^{\infty} D_3^n r^n P_n^1(\cos\theta)\cos\phi, \tag{33b}$$

where D_i^n are the unknown coefficients for the temperature field expansion for the ith fluid and the $P_n^1(\cdot)$'s are the normalized associated Legendre functions.

The general solution to the Stokes equation (1) in spherical coordinates is known as Lamb's solution and is based on the spherical harmonic expansion for the pressure field. Employing the requirements on the asymptotics (15a), boundedness, and symmetry analogous to the temperature field allows us to reduce Lamb's solution to

$$V_{ir} = \frac{V_{ir}^{\infty} - U_0\sin\theta\cos\phi}{v_0} + \sum_{n=1}^{\infty}\left(A_i^n \frac{n+1}{2\alpha_1(2n-1)} - B_i^n\frac{n+1}{r^2}\right) r^{-n} P_n^1\cos\phi, \tag{34a}$$

$$V_{i\theta} = \frac{V_{i\theta}^{\infty} - U_0\cos\theta\cos\phi}{v_0} + \sum_{n=1}^{\infty}\left(A_i^n\frac{2-n}{2\alpha_1 n(2n-1)}\frac{dP_n^1}{d\theta} + B_i^n\frac{1}{r^2}\frac{dP_n^1}{d\theta} + C_i^n\frac{P_n^1}{r\sin\theta}\right) r^{-n}\cos\phi, \tag{34b}$$

$$V_{i\phi} = \frac{V_{i\phi}^{\infty} + U_0\sin\phi}{v_0} + \sum_{n=1}^{\infty}\left(A_i^n\frac{(n-2)P_n^1}{2\alpha_1 n(2n-1)\sin\theta} - B_i^n\frac{P_n^1}{r^2\sin\theta} - C_i^n\frac{1}{r}\frac{dP_n^1}{d\theta}\right) r^{-n}\sin\phi, \tag{34c}$$

$$p_i = \sum_{n=1}^{\infty} A_i^n P_n^1 r^{-n-1}\cos\phi, \tag{34d}$$

for the nondimensional exterior velocity and pressure fields, $i=1$, 2, and

$$V_{3r} = \sum_{n=1}^{\infty}\left(A_3^n\frac{nr}{2\alpha_3(2n+3)} + B_3^n\frac{n}{r}\right) r^n P_n^1\cos(\phi), \tag{35a}$$

$$V_{3\theta} = \sum_{n=1}^{\infty}\left(A_3^n\frac{n+3}{2\alpha_3(n+1)(2n+3)}\frac{dP_n^1}{d\theta} + B_3^n\frac{1}{r}\frac{dP_n^1}{d\theta} + C_3^n\frac{P_n^1}{\sin\theta}\right) r^n\cos(\phi), \tag{35b}$$

$$V_{3\phi} = \sum_{n=1}^{\infty}\left(A_3^n\frac{-(n+3)rP_n^1}{2\alpha_3 n(2n+3)(n+1)\sin\theta} - B_3^n\frac{P_n^1}{r\sin\theta} - C_3^n\frac{dP_n^1}{d\theta}\right) r^n\sin(\phi), \tag{35c}$$

$$p_3 = \frac{2r_0}{R_2 Ca_2} + \sum_{n=1}^{\infty} A_3^n P_n^1 r^n\cos(\phi) \tag{35d}$$

for the nondimensional interior velocity and pressure fields, where A_i^n, B_i^n, and C_i^n are the unknown expansion coefficients. For brevity, the $\cos\theta$ dependence of the associated Legendre functions was omitted.

Note that these general solutions automatically satisfy the boundary conditions at the walls of the container, but not at the fluid-fluid interfaces $\partial\Omega_{ij}$. In particular, Eq. (34) satisfies the no-slip boundary condition at the solid bottom boundary in the limit $r_0 \ll H$ considered here. In this limit we also have $|d| \ll H$, so that near the droplet the asymptotic flow field (12c) in the substrate simplifies to

$$\mathbf{V}_2^{\infty} = \frac{\sigma_{12}'\Theta}{\mu_2}\left(z - d + \frac{H}{4}\right)\hat{\mathbf{x}}. \tag{36}$$

B. Force on the droplet

The force on the droplet is linear in the velocity and temperature fields and hence can be represented as a linear function of the expansion coefficients. The contact line force (32) can be computed analytically by substituting the expansion for the temperature field at the contact line and evaluating the integral. Due to the continuity of the temperature field, any one of the three expansions (33) can be used. For simplicity we have chosen to use the interior field (33b):

$$\mathbf{f}_{\text{line}} = -\pi\tau_{12} r_c\sin\theta_c \sum_{n=1}^{N} D_3^n r_c^n P_n^1(\cos\theta_c)\hat{\mathbf{x}}. \tag{37}$$

The surface force (30) can be broken up into two contributions: the force due to the asymptotic velocity field $\mathbf{V}^{\infty}$ and the force due to the correction $\mathbf{V}^* = \mathbf{V} - \mathbf{V}^{\infty}$ arising due to the presence of the droplet. The first contribution can again be computed analytically:

$$\mathbf{f}_{\text{surface}}^{\infty} = \pi\tau_{12}(r_c\sin\theta_c)^2\hat{\mathbf{x}}. \tag{38}$$

If the interface $\partial\Omega_{12}$ is chosen to coincide with the plane $z=0$ (i.e., if $d=0$), the second contribution can also be computed analytically using the property of Stokes flow that its stress tensor has zero divergence. Applying the Stokes theorem to transform the integral over the drop surface (30) to an integral over two hemispheres at infinity and the $z=0$ plane, we find

$$\mathbf{f}^*_{\text{surface}} = \left[\pi\sqrt{3}(A_1^1 + A_2^1) + \sum_{n=1}^{N} \pi r_c^{-n+1} \left.\frac{dP_n^1}{d\theta}\right|_{\theta=\theta_c} \times \frac{n^2+1-n}{(n-1)(2n-1)n}(A_1^n - A_2^n) - \sum_{n=1}^{N} 2\pi r_c^{-n-1} \left.\frac{dP_n^1}{d\theta}\right|_{\theta=\theta_c} \cdot (\alpha_1 B_1^n - B_2^n) - \sum_{n=1}^{N} \pi \frac{r_c^{-n}}{n} \left((n+1)P_n^1 - \frac{d^2P_n^1}{d\theta^2} \right)_{\theta=\theta_c} \times (\alpha_1 C_1^n - C_2^n) \right] \hat{\mathbf{x}}. \quad (39)$$

If the interface $\partial\Omega_{12}$ does not lie in the $z=0$ plane, $\mathbf{f}^*_{\text{surface}}$ has to be computed differently. Integration over ϕ can still be carried out analytically. The integration over the θ domain cannot and is done numerically using an adaptive recursive Simpson's rule scheme. Evaluation of the numerical prefactors for each of the unknown expansion coefficients in Lamb's solution, above and below the drop, requires $6N$ integrals to be evaluated, which becomes the costliest component of the numerical procedure.

C. Numerical solution

Since the shape of all the free interfaces is already determined, we do not need to satisfy the normal stress balance boundary condition (7b) at every point on every interface. Therefore, the unknown coefficients A_i^n, B_i^n, C_i^n, D_i^n, and U_0 can be determined by substituting expansions (33)–(35) into boundary conditions (3), (4), and (7a), and imposing the zero force constraint (29). Our method for solving the resulting system of equations is based on the boundary collocation procedure of Hassonjee *et al.*,[28] which is itself a development of the approach proposed by Ganatos *et al.*[29] The expansions for the temperature and velocity fields are first truncated to N terms. The resulting equations are linear in either $\sin\phi$ or $\cos\phi$, so that the ϕ-dependence can be immediately factored out. This results in a system of equations that depend only on θ. Each equation is then evaluated on a grid of θ values, referred to as collocation rings. We choose a total of M collocation rings covering all three fluid-fluid interfaces. Since $\partial\Omega_{12}$ is unbounded, the largest ring is placed at a finite distance $s_{\max}$ from the z axis.

The zero force constraint together with the boundary conditions evaluated on the collocation rings defines a system of linear equations with constant coefficients. Given N, we choose M large enough to make the system overdetermined, so that the number of equations $(8M+1)$ exceeds the number of unknowns $(12N+1)$. The resulting system is solved in a least-squares sense using MATLAB's implementation of LAPACK which utilizes householder reflections for computing an orthogonal-triangular factorization.

To gauge the accuracy of our boundary collocation scheme we define the residual of our system of equations

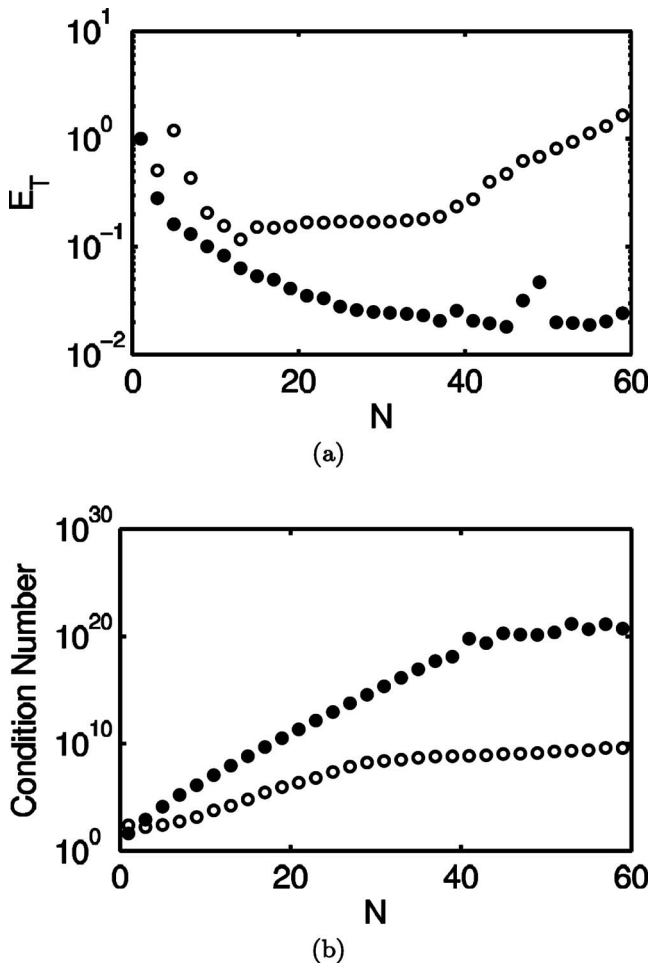

FIG. 3. The dependence of the residual E_T (a) and condition number (b) on the truncation order N without preconditioning (filled circles) and with preconditioning (open circles). The dimensionless parameters of Table I are all set to one except $\gamma_{12}=0.5$ (the corresponding droplet shape is shown in Fig. 7).

$$E_T = \left[f^2 + \sum_{i,j,k} \int_{\partial\Omega_{jk}} |\Delta_{ijk}|^2 dS_{jk} \right]^{1/2}, \quad (40)$$

where dS_{jk} is the area element of the interface $\partial\Omega_{jk}$. Δ_{ijk} is the error in the ith boundary condition at the interface $\partial\Omega_{jk}$ and f is the total force on the droplet, each evaluated using our truncated solutions for the temperature and velocity fields.

For a given set of dimensionless parameters, our numerical solution can depend on the choice of N, M, and $s_{\max}$, as well as on the distribution of the collocation rings. However, for sufficiently large N, we expect the numerical solution to converge to the exact one, with the residual approaching zero. We chose to use the minimum values for N, M, and $s_{\max}$ that minimize E_T. For a generic choice of dimensionless parameters, we found that using values of $N=50$, $M=675$, and $s_{\max}=9$ decreases the residual by two orders of magnitude compared to that for $N=1$ (with the same values of M and $s_{\max}$) as Fig. 3(a) illustrates. These are the default values used in all of the calculations reported here, unless specified otherwise.

Several different distributions for the collocation rings were tested. Ultimately a distribution with equal spacing in θ for $\partial\Omega_{13}$ and $\partial\Omega_{23}$ was chosen. For the rings on the interface $\partial\Omega_{12}$ equal distance spacing was used. It was found that this distribution has a slight advantage in terms of the residuals and conditioning over other distributions (such as the abscissa for a Gauss–Legendre quadrature rule or equal area spacing).

The major difference between the implementation of the boundary collocation method presented here and the one developed by Ganatos *et al.*[29] is the total number of collocation rings M used when finding a solution. Recall that the collocation rings correspond to discrete values of θ. Any function expanded in powers of cos θ (e.g., spherical harmonics), will possess multiple values of θ that result in identical function values. To obtain the number of equations equal to the number of unknowns, Ganatos *et al.* invested considerable effort in determining which values of θ, for given M and N, would result in a degenerate system and consequently should be avoided. For large values of N this task becomes impractical.

In our approach, the difficulties in constructing a square system are sidestepped by generously overdetermining the system of equations. For example, for the default choice of N and M there are nearly seven equations for every unknown in the linear system. The trade-off is that solving such a large system is computationally more expensive, although still well within the capabilities of a modern desktop computer.

The limit to the accuracy of the boundary collocation scheme was found to be set by the poor conditioning of the system at very large truncation orders. The condition number (the ratio of the largest singular value to the smallest) determines the stability of the system with respect to inversion (i.e., computing the inverse of the linear system). Typically, one finds a nearly exponential growth of the condition number of the coefficient matrix with N, as Fig. 3(b) shows for a near-spherical symmetric droplet.

The most fundamental reason for the poor conditioning is the loss of orthogonality of the discretized associated Legendre functions, used as basis functions, at large N. Sneeuw[30] demonstrated that orthogonality can be restored by multiplying each $P_n^m(x_i)$ by a unique weight associated with each x_i. Sneeuw found that this significantly improved the condition number and allowed for a much larger truncation order than was previously possible in similar problems.

In an attempt to correct for the lost orthogonality of the Legendre functions, preconditioning of the coefficient matrix and a rescaling of the unknowns was tested. Direct implementation of Sneeuw's method to our numerical procedure is impossible: Sneeuw was fitting collocation points with associated Legendre functions alone. The basis functions (i.e., Lamb's solution) used in our collocation scheme are comprised of associated Legendre functions and their derivatives. This prevents us from determining a unique weight associated with each term in Lamb's solution. Instead we developed a preconditioning scheme that would weigh each row and column of our linear system with a unique weight defined in a manner analogous to Sneeuw's method.

As Fig. 3(b) illustrates, preconditioning reduces the condition number by many orders of magnitude. However, it was also found that preconditioning leads to a dramatic increase in the residual and an early loss of convergence in N, as Fig. 3(a) illustrates. Preconditioning of the linear system was therefore not implemented. On the other hand, it was found that placing the origin at the center of mass of the droplet always resulted in the lowest possible condition number. Hence, this choice was used in all the calculations reported in this paper.

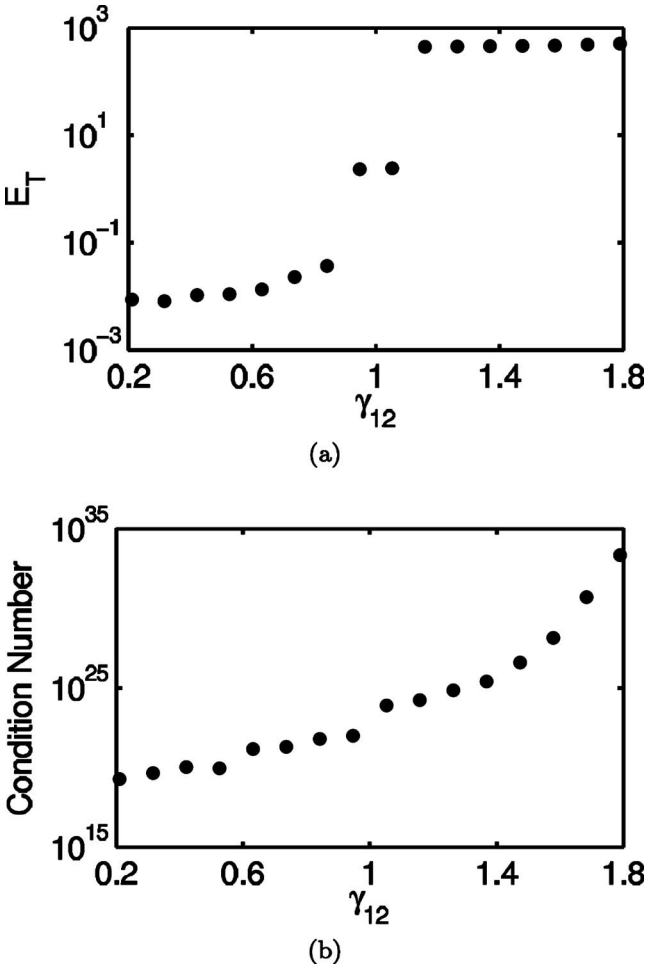

FIG. 4. The dependence of the residual E_T (a) and condition number (b) on the droplet aspect ratio ($\gamma_{12}=0$ corresponds to spherical droplet and $\gamma_{12}=2$ to a slender film).

Not surprisingly, it was found that conditioning is also substantially affected by the shape of the droplet. In part, this is due to the evaluation of interior and exterior fields at the interfaces $\partial\Omega_{13}$ and $\partial\Omega_{23}$, characterized by a varying distance from the origin. Since the highest order terms in the expansions for the inner fields scale as r^N and those for the exterior fields scale as r^{-N}, the entries of the coefficient matrix vary by $\mathcal{O}[(r_{\max}/r_{\min})^N]$.

As Fig. 4(b) illustrates, the condition number becomes very large for slender droplets, like that shown in Fig. 2(b). As a result, the boundary collocation scheme fails to produce an accurate solution at high truncation orders for slender droplets, as Figs. 4(a) and 5(a) show. Furthermore, Fig. 5(a) shows that our boundary collocation scheme also has difficulties at higher truncation orders for highly asymmetric

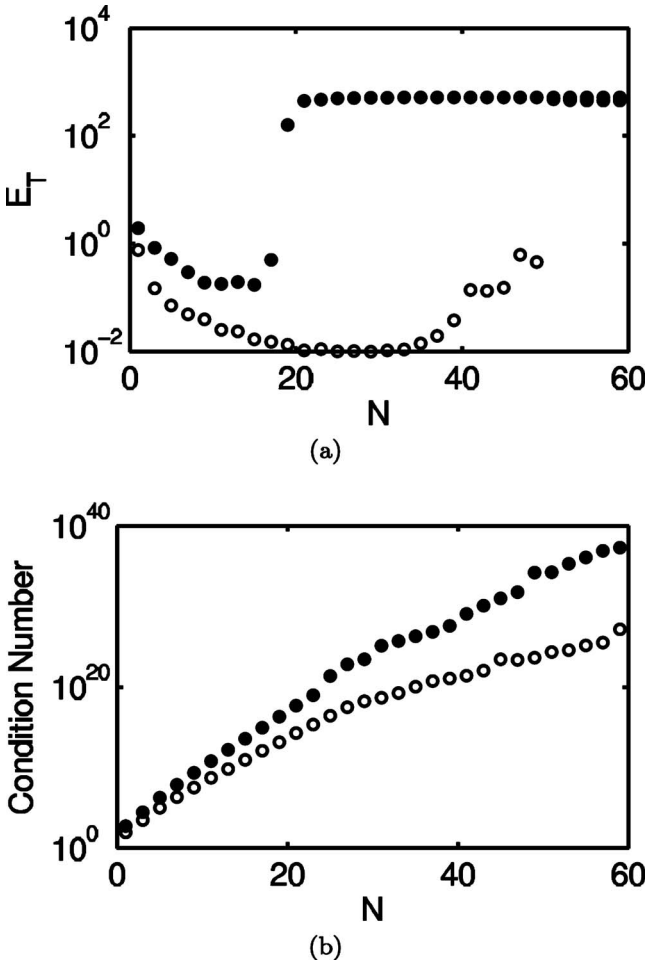

FIG. 5. The dependence of the residual E_T (a) and condition number (b) on the truncation order. Filled circles correspond to a slender symmetrical droplet shown in Fig. 2(b). Open circles correspond to a strongly asymmetric droplet shown in Fig. 2(c).

droplets such as that shown in Fig. 2(c) (although $N=20$ already produces a solution with an acceptably small residual).

In either case, the reason for the increase in the residual can be traced to the poor conditioning of the linear system [see Figs. 4(b) and 5(b)], such that increasing a truncation order N beyond a certain limit reduces, rather than improves, the accuracy of the numerical solution. The underlying reason is that, although Lamb's solution is based on a complete set of basis functions, it is ill suited for geometries deviating significantly from spherical.

D. Code validation

To test our boundary collocation scheme, we solved the linear system with parameters chosen to represent a spherical drop immersed in an infinite layer of fluid with an imposed constant temperature gradient. This is achieved by setting $\gamma_{12}=\tau_{12}=0$ and $\alpha_1=\beta_1=\gamma_{13}=\tau_{13}=1$. The problem has a well-known analytical solution,[31] with the corresponding velocity field (in the reference frame moving with the droplet) known as Hill's spherical vortex

TABLE II. The coefficients of Lamb's expansions (34) and (35) of the interior and exterior flow field for thermocapillary migration of a completely submerged droplet for $\alpha_3=1$, $\beta_3=1$ (all nonzero coefficients are shown). The column labeled "theory" corresponds to the analytical solution (41) and the column labeled "error" shows the difference between the analytical and the numerical solution.

Coefficient	Theory	Error
A_1^1	0.000 000e+00	3.050 723e−15
B_1^1	7.698 004e−02	6.208 527e−11
C_1^1	0.000 000e+00	4.976 496e−11
A_2^1	0.000 000e+00	4.298 810e−15
B_2^1	7.698 004e−02	6.212 796e−11
C_2^1	0.000 000e+00	4.976 601e−11
A_3^1	2.309 401e+00	1.465 494e−14
B_3^1	−3.849 002e−01	2.164 935e−15
C_3^1	0.000 000e+00	4.312 644e−12

$$V_{3r}=-3\frac{\sin(\theta)\cos(\phi)(r^2-1)}{(3\alpha_3+2)(\beta_3+2)}, \tag{41a}$$

$$V_{3\theta}=-3\frac{(-1+2r^2)\cos(\theta)\cos(\phi)}{(3\alpha_3+2)(\beta_3+2)}, \tag{41b}$$

$$V_{3\phi}=3\frac{(-1+2r^2)\sin(\phi)}{(3\alpha_3+2)(\beta_3+2)}, \tag{41c}$$

and

$$V_{1r}=V_{2r}=-2\frac{(r^3-1)\sin(\theta)\cos(\phi)}{(\beta_3+2)(3\alpha_3+2)r^3}, \tag{41d}$$

$$V_{1\theta}=V_{2\theta}=-\frac{(2r^3+1)\cos(\theta)\cos(\phi)}{(\beta_3+2)(3\alpha_3+2)r^3}, \tag{41e}$$

$$V_{1\phi}=V_{2\phi}=\frac{(2r^3+1)\sin(\phi)}{r^3(3\alpha_3+2)(\beta_3+2)}. \tag{41f}$$

The computed numerical solutions for the temperature and velocity fields for different values of the two remaining dimensionless parameters, viscosity ratio α_3 and thermal conductivity ratio β_3, show excellent agreement with this analytical solution (see, e.g., Table II).

To further illustrate the agreement between the numerical and analytical solutions we compare the thermocapillary migration velocity obtained numerically with the analytical result originally derived by Young *et al.*[1] which, in dimensional units, is

$$U_{\mathrm{YGB}}=-\frac{2r_0k_2\sigma'_{23}\Theta}{(2\mu_2+3\mu_3)(2k_2+k_3)} \tag{42}$$

or, after nondimensionalization,

$$u_s\equiv\frac{U_{\mathrm{YGB}}}{v_0}=\frac{2}{(2+3\alpha_3)(2+\beta_3)}. \tag{43}$$

As Fig. 6 illustrates, the numerical solution agrees very well with the analytical one for all values of α_3 and β_3 considered.

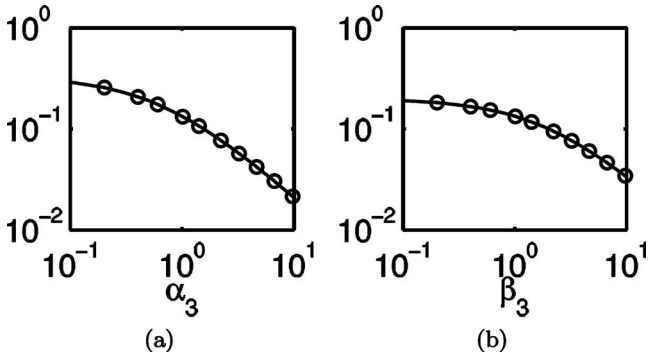

FIG. 6. The migration velocity dependence on α_3 with $\beta_3=1$ (a) and on β_3 with $\alpha_3=1$ (b). The solid curves correspond to analytical solution (43) and the symbols represent solutions found numerically.

IV. RESULTS AND DISCUSSION

Next we use the boundary collocation method described previously to determine the velocity of thermocapillary migration for interfacial droplets and the flow fields, inside and outside the droplet, arising in response to the applied temperature gradient.

A. Temperature field

Although the temperature field is not of direct interest here, it is important for describing the relative magnitudes of thermocapillary stresses at the surfaces of the droplet and the substrate. Qualitatively, the structure of the temperature field is controlled by the thermal conductivity ratios β_1 and β_3.

In particular, $\beta_1=k_1/k_2$ controls the relative magnitude (and uniformity) of the thermocapillary stresses at the droplet's top and bottom surface. As Figs. 7(a) and 7(b) illustrate, for $\beta_1<1$ the temperature gradient at the top of the droplet is smaller, while for $\beta_1>1$ it is larger, than at the bottom. Correspondingly, the thermocapillary stresses at the top dominate for $\beta_1>1$ and those at the bottom dominate for $\beta_1<1$. It should be mentioned that, although the overall temperature drop across the top and the bottom cap is exactly the same regardless of β_1 ($T_1=T_2=T_3$ everywhere on the contact line), it is the regions near the top and the bottom of the droplet that have the largest contribution to the surface force (30).

The second ratio $\beta_3=k_3/k_2$ controls the importance of thermocapillary stresses at the droplet surface relative to those at the substrate surface. Figures 7(c) and 7(d) show that for $\beta_3<1$ the thermal gradient at the droplet surface increases above its value at the substrate surface away from the droplet, while for $\beta_3>1$ the thermal gradient on the droplet surface decreases below that value. In particular, for $\beta_3\to\infty$ the temperature becomes constant throughout the droplet and the thermocapillary stress on the droplet surface vanishes.

The remaining parameters that affect the temperature field are those that define the droplet shape. We found that varying these parameters always resulted in a temperature field that resembled one of the four types shown in Fig. 7.

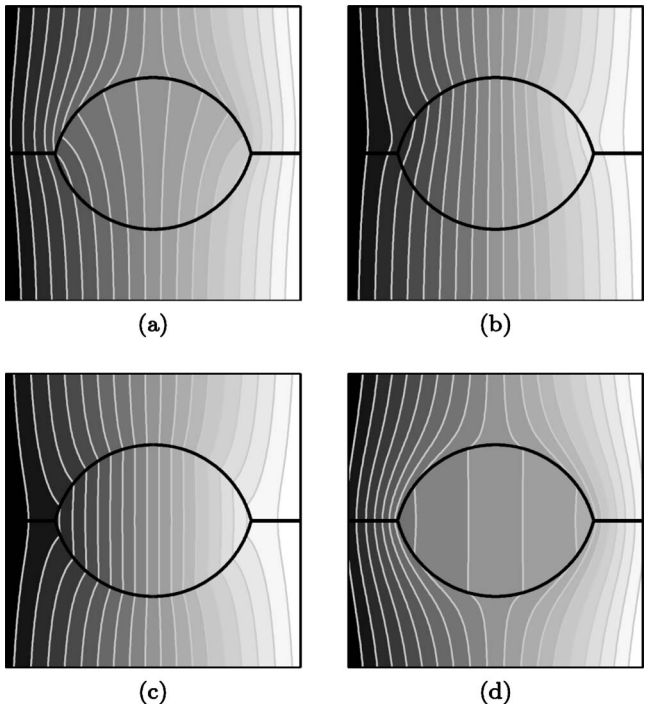

FIG. 7. Temperature field in the $y=0$. The darker shading corresponding to cooler fluid with 20 isotherms evenly spaced over the range of temperature $[-T_{\max},T_{\max}]$. The parameters are $\gamma_{12}=0.5$, $\gamma_{13}=1$ and (a) $\beta_1=0.09$, $\beta_3=1$, $T_{\max}=1.66$, (b) $\beta_1=10$, $\beta_3=1$, $T_{\max}=1.78$, (c) $\beta_3=0.09$, $\beta_1=1$, $T_{\max}=1.84$, and (d) $\beta_3=10$, $\beta_1=1$, $T_{\max}=1.60$.

B. Thermocapillary migration velocity

In the classical problem of thermocapillary migration, the droplet velocity (42) is essentially determined by the thermocapillary effect at the droplet surface, with the substrate fluid being essentially at rest far from the droplet. For substrates with a free surface, the substrate itself comes in motion due to the thermocapillary effect at its free surface. The characteristic velocity due to the thermocapillary effect at the substrate surface is $V_1^\infty\sim\chi v_0$ (in the $-\hat{\mathbf{x}}$ direction), while that due to the thermocapillary effect at droplet surface is v_0 (in the $+\hat{\mathbf{x}}$ direction), smaller by a factor of $\chi=H/r_0$. Since for interfacial droplets the ratio χ is typically quite large, the dominant contribution to the thermocapillary migration speed U_0 is given by the advection of the droplet by the substrate flow (12b) rather than the thermocapillary effect at the droplet surface. Moreover, an interfacial droplet would move in the direction opposite to the applied temperature gradient, while the classical thermocapillary migration is in the direction of the gradient.

Since the contribution of the thermocapillary effect on the droplet surface is much smaller than that on the substrate surface, the variation in the thermocapillary migration velocity with parameters is the easiest to describe in terms of the mobility function

$$M_i\equiv\frac{U_0-V_1^\infty}{U_{\mathrm{YGB}}},\tag{44}$$

where V_1^∞ is the velocity of the asymptotic flow at the substrate surface. The mobility function represents the magni-

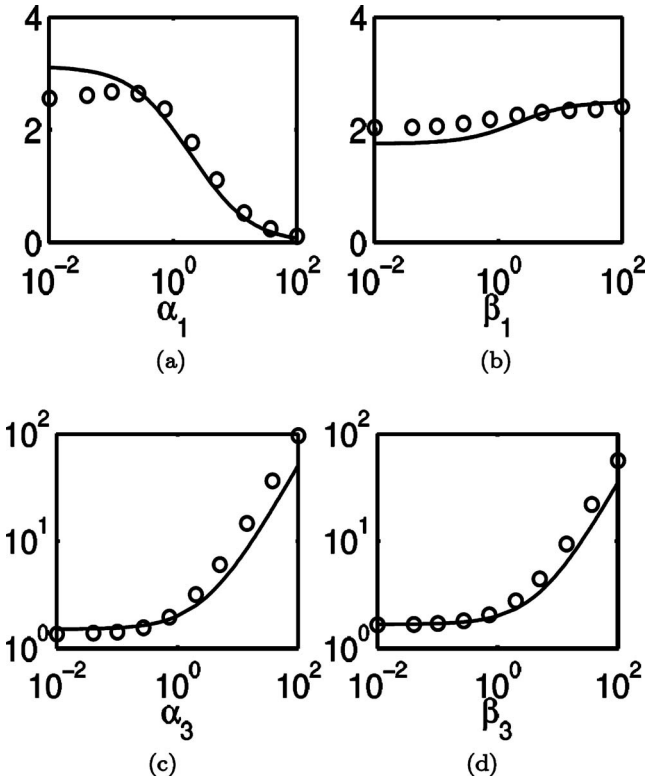

FIG. 8. The mobility function dependence on the bulk material parameters. The symbols show the numerical results for the interfacial droplet and the solid curve estimate (48).

tude of the thermocapillary migration speed of an interfacial droplet, with the advection component subtracted off, relative to the classical thermocapillary migration velocity. Deviations of M_i from unity demonstrate the effects of confinement at an interface, the droplet shape variation, and the discontinuity in the physical properties of the surrounding fluid on thermocapillary migration speed in a form independent of the substrate depth H and the droplet size r_0.

There are too many nondimensional parameters to explore the migration velocity of an interfacial droplet comprehensively. Therefore, we chose to restrict our focus to the dependence of the mobility function M_i on each of the eight $O(1)$ nondimensional parameters, with the other seven held fixed. All the fixed parameters were set to unity except γ_{12}, the nondimensional surface tension at the interface $\partial\Omega_{12}$. A value of $\gamma_{12}=0.5$ was chosen to yield an interfacial droplet with moderate, compared to a perfect sphere, deformation (see Fig. 7).

We start by examining the dependence on the bulk properties of the fluids, the viscosity and thermal conductivity ratios. As Fig. 8(a) illustrates, an increase in the viscosity ratio $\alpha_1=\mu_1/\mu_2$ results in a decrease in M_i. This trend is due to the increased viscous drag at the top cap of the droplet for large α_1: as μ_1 increases with all other parameters fixed, $U_0-V_1^{\infty}$ decreases, while U_{YGB} does not change.

A more quantitative description can be obtained by representing the migration velocity as a sum of three components

$$U_0 = V_1^{\infty} + U_{\mathrm{tc}} + U_{\mathrm{sh}}, \tag{45}$$

where V_1^{∞} describes the advection by the asymptotic flow, U_{tc} is a correction due to the thermocapillary effect at the droplet surface, and U_{sh} is a correction due to the shear in the substrate fluid (which is itself a result of the thermocapillary effect at the substrate interface $\partial\Omega_{12}$). The component U_{tc} can be estimated by using a modification of the classical expression (42), where the material parameters describing the fluid surrounding the droplet are replaced with the averages of the corresponding parameters for fluids 1 and 2:

$$U_{\mathrm{tc}} = -\frac{r_0\Theta(\sigma'_{13}+\sigma'_{23})(k_1+k_2)}{2(\mu_1+\mu_2+3\mu_3)(k_1+k_2+k_3)}. \tag{46}$$

The contribution U_{sh} can be estimated by adapting the expression for the sedimentation velocity of a liquid droplet; the well-known Hadamard–Rybczyński problem[32,33]

$$U_{\mathrm{sh}} = -C\frac{r_0\Theta\sigma'_{12}(\mu_1+\mu_2+2\mu_3)}{2\mu_2(\mu_1+\mu_2+3\mu_3)}, \tag{47}$$

where C is a geometric factor describing the degree of submersion of the droplet into the substrate fluid and the values of material parameters for the surrounding fluid were replaced with the averages of those for fluids 1 and 2. Substituting these expressions into the definition of the mobility function one obtains

$$M_i^{\mathrm{est}} = \frac{(1+\tau_{13})(2+3\alpha_3)(1+\beta_1)(2+\beta_3)}{4(1+\alpha_1+3\alpha_3)(1+\beta_1+\beta_3)} + C\frac{\tau_{12}(1+\alpha_1+2\alpha_3)(2+3\alpha_3)(2+\beta_3)}{2(1+\alpha_1+3\alpha_3)(1+\alpha_1)}. \tag{48}$$

Comparing the numerical result with estimate (48) we find rather good agreement, except for a small decrease in M_i at $\alpha_1\to 0$, which is likely due to a subtle flow rearrangement around the droplet. Here and below we set $C=1/3$. This value of C was chosen such that, when all parameters are set to one, both terms in Eq. (48) are equal to unity. In effect, this sets the nondimensionalized versions of Eqs. (46) and (47), the thermocapillary and shear corrections to the migration velocity, equal to each other when the material parameters of the substrate and covering fluid are equal.

The dependence of M_i on the thermal conductivity ratio $\beta_1=k_1/k_2$ shown in Fig. 8(b) is also in reasonable agreement with estimate (48). As k_1 is increased (decreased), with all other parameters fixed, the thermocapillary effect at the top of the droplet starts to dominate (lag) that at the bottom (recall the discussion in Sec. IV A), leading to an increase (decrease) in the thermocapillary migration speed of the droplet relative to the substrate fluid(s). The dependence on β_1 is rather weak, reflecting the weak dependence of the thermal gradients on β_1 (see Fig. 7).

The dependence of M_i on the viscosity ratio $\alpha_3=\mu_3/\mu_2$ is shown in Fig. 8(c). We again find reasonable agreement with Eq. (48) for all values of α_3. For small α_3, M_i approaches a constant. In the limit $\alpha_3\to\infty$ (or $\mu_3\to\infty$ with all other parameters fixed) both U_{YGB} and U_{tc} vanish; the thermocapillary migration speed of the droplet relative to the

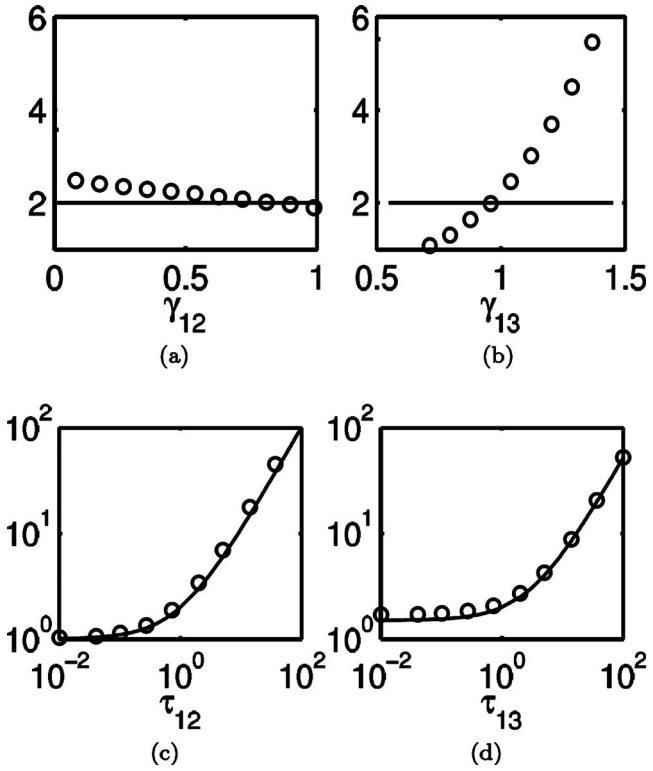

FIG. 9. The mobility function dependence on the interfacial material parameters. The symbols show the numerical results for the interfacial droplet and the solid curve estimate (48).

substrate is dominated by the shear flow in the substrate and approaches a constant. In this limit Eq. (48) yields $M_i \sim \alpha_3$. The dependence of M_i on the thermal conductivity ratio $\beta_3 = k_3/k_2$ [see Fig. 8(d)] can be understood using the same argument, which predicts M_i=const for small β_3 and $M_i \sim \beta_3$ for large β_3.

The same argument also explains the dependence of M_i on the surface tension temperature coefficient ratio $\tau_{12} = \sigma'_{12}/\sigma'_{23}$ shown in Fig. 9(c). Here Eq. (48) predicts M_i=const for small τ_{12} when the thermocapillary effect at the interface $\partial\Omega_{12}$ is negligible. Note that the numerical computation yields $M_i \approx 1$ for $\tau_{12} \to 0$ (just as it should be for a nearly spherical droplet when $U_{tc} \approx U_{YGB} \gg U_{sh}$). For large τ_{12} when the thermocapillary effect at the interface $\partial\Omega_{12}$ is dominant, Eq. (48) yields $M_i \sim \tau_{12}$, in agreement with the numerical result.

The dependence of the mobility function on the second surface tension temperature coefficient ratio $\tau_{13} = \sigma'_{13}/\sigma'_{23}$ is shown in Fig. 9(d). It is also accurately described by estimate (48) for all values of τ_{13} and can be understood using the same arguments used previously to explain the dependence on β_1.

We conclude this section by discussing the dependence of the mobility function on the surface tension ratios $\gamma_{12} = \bar{\sigma}_{12}/\bar{\sigma}_{23}$ and $\gamma_{13} = \bar{\sigma}_{13}/\bar{\sigma}_{23}$. These ratios determine the droplet shape and position relative to the substrate surface $\partial\Omega_{12}$ (see Sec. II D). No simple analytical argument can be used to predict this dependence quantitatively, so one has to resort to qualitative arguments. In particular, as γ_{12} increases from zero, the droplet shape deviates progressively from a

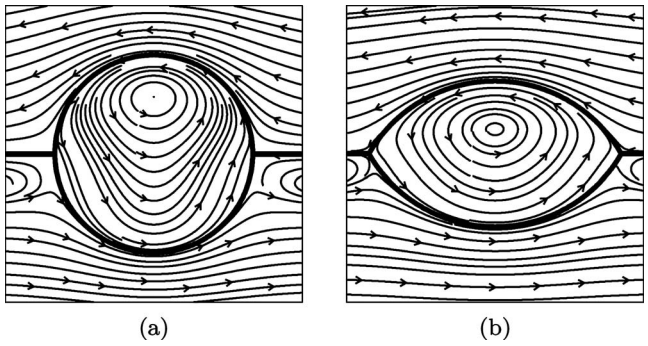

FIG. 10. The droplet shape and streamlines of the flow in the y=0 plane. The value of the surface tension ratio γ_{12}=0 corresponds to a spherical droplet (a) and γ_{12}=1 results in a slender droplet (b). All other parameters are fixed at unity.

sphere to a slender symmetric (for γ_{13}=1) liquid lens (see Fig. 10). The resulting increase in the surface-to-volume ratio leads to an increase in the viscous drag and a corresponding decrease in the contribution of the thermocapillary effect on the droplet surface to the migration speed, leading to a decrease in U_{tc} and hence M_i [see Fig. 9(a)].

The value of γ_{13} controls the position of the droplet relative to the substrate surface and hence the value of the geometrical prefactor C in Eq. (47). For small γ_{13} the droplet is almost completely expelled by the substrate fluid into the covering fluid [see Fig. 11(b)], C is small, so the shear flow in the substrate fluid has almost no contribution to the thermocapillary migration speed, $U_{sh} \ll U_{tc} \approx U_{YGB}$. In this limit one should expect $M_i \approx 1$, as the numerics confirm. As γ_{13} increases, so does the immersion into the substrate fluid, the prefactor C, and hence U_{sh}, explaining the trend observed in Fig. 9(b). For large γ_{13} [see Fig. 11(a)] the droplet is almost completely encapsulated by the substrate, with M_i achieving near-maximal values.

C. Interior flow field

Next we turn to the description of the flow field inside interfacial droplets. As we mentioned previously, the topological structure of this flow field is crucially important for determining its mixing properties. It is the easiest to characterize this topological structure by identifying the invariant

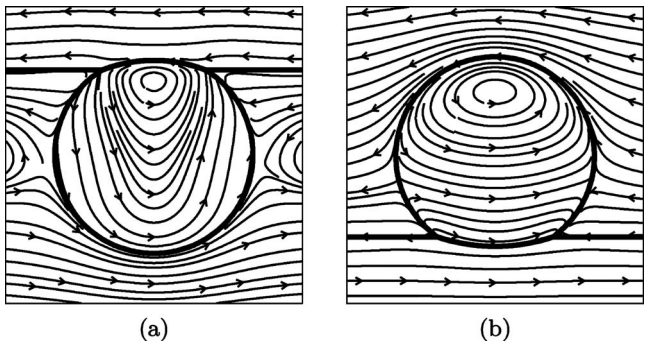

FIG. 11. The droplet shape and streamlines in the y=0 plane. The droplet is almost completely encapsulated by the substrate for γ_{13}=1.45 (a) and almost completely expelled for γ_{13}=0.55 (b). In both cases γ_{12}=0.5 and all other parameters are set to unity.

sets of the flow such as separatrix surfaces, homo- and heteroclinic orbits, and fixed points of the flow. One question of particular interest is whether the deviation of the droplet shape from a sphere, and the associated discontinuity in the surface curvature at the contact line, have a significant impact on the flow topology, as compared with the flow in a completely submerged spherical droplet under similar conditions.

1. Comparison with the model

To gain a better understanding of the flow structure for generic values of parameters we will compare the numerically computed solution for the interfacial droplet with the analytical one produced by a simplified model of the flow derived in Ref. 21. In the analytical model, a spherical droplet was assumed to be completely submerged (with its center at a fixed distance $d \geq r_0$ below the interface) in the substrate fluid, hence we will refer to this system as a submerged droplet. In the model the interior velocity was assumed to be given by a linear superposition of the $n=1$ and $n=2$ terms in Lamb's solution (35), the first one representing the dipolelike field (Hill's spherical vortex) arising due to the thermocapillary effect on the droplet surface and the second—a recirculation flow (referred to as the Taylor flow in Ref. 21) caused by the shear flow (12c) in the substrate fluid. In our notations the nondimensionalized interior velocity field of the submerged droplet is

$$v_r = 3(1-r^2)\left(\frac{r\cos\theta}{2\alpha_3+2}\tau_{12} + \frac{1}{(3\alpha_3+2)(2+\beta_3)}\right)\sin\theta\cos\phi, \tag{49a}$$

$$v_\theta = \left(\frac{r[(6-10r^2)\cos^2\theta - 5(1-r^2) - 2\alpha_3]}{4\alpha_3+4}\tau_{12} + \frac{3(1-2r^2)\cos\theta}{(3\alpha_3+2)(2+\beta_3)}\right)\cos\phi, \tag{49b}$$

$$v_\phi = -\left(\frac{r(1-5r^2-2\alpha_3)\cos\theta}{4\alpha_3+4}\tau_{12} + \frac{3(1-2r^2)}{(3\alpha_3+2)(2+\beta_3)}\right)\sin\phi. \tag{49c}$$

The problem has the same symmetry in the presence of a constant horizontal temperature gradient, regardless of whether the droplet is fully submerged or is suspended at the surface of the substrate. The flow is mirror symmetric with respect to the $y=0$ plane, which is thus both an invariant plane and a separatrix of the flow, with $V_y=0$ at $y=0$. Another separatrix surface is the droplet surface. The flow is also invariant with respect to reflection about the $x=0$ plane combined with time reversal ($\mathbf{v}\to-\mathbf{v}$), so that $v_y=v_z=0$ at $x=0$. Combined with the incompressibility condition (1), this guarantees the existence of a line of fixed points of the flow, where $\mathbf{v}=0$, lying in the plane $x=0$. We will, therefore, concentrate on the velocity field in the planes $x=0$ and $y=0$ which contain the majority of invariant sets.

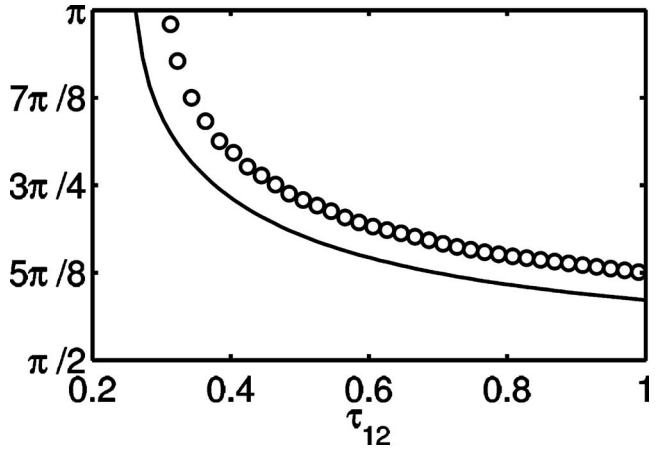

FIG. 12. The polar angle of the fixed points on the surface of the submerged (solid line) and the interfacial drop (circles) restricted to the $x=0$ plane.

In particular, flow (49) possesses a set of (saddle) fixed points lying at the intersection of the $y=0$ plane with the droplet surface, with the polar angle given by

$$\frac{\tau_1(2\cos^2\theta+\alpha_3)}{2(\alpha_3+1)} + \frac{3\cos\theta}{(3\alpha_3+2)(2+\beta_3)} = 0. \tag{50}$$

Another set of (elliptic) fixed points lies at the intersection of the droplet surface with the $x=0$ plane, with the polar angle given by

$$\frac{\tau_1(\alpha_3+2)\cos\theta}{2(\alpha_3+1)} + \frac{3}{(3\alpha_3+2)(2+\beta_3)} = 0. \tag{51}$$

To calculate the locations of the fixed points for the interfacial drop we chose the values of relative surface tensions $\gamma_{12}=1$ and $\gamma_{13}=1.888$ for which the interfacial droplet is almost completely submerged. (Choosing a larger value of γ_{13} results in a solution with an unacceptably large residual.) We also set $\alpha_3=1$ and $\alpha_1=0$ to reflect the fact that in practice the covering fluid (e.g., air or even vacuum) would typically have viscosity negligible compared to that of both the droplet and the substrate. The thermal conductivity of a typical covering fluid would also be small. However, we chose to set $\beta_1=\beta_3=1$ to make the temperature gradient at the droplet surface uniform, in accordance with the assumption used in deriving the model.

The numerical results for various relative temperature coefficients of surface tension τ_{12}, with fixed $\tau_{13}=1$, are found to be in a good qualitative (and often even quantitative) agreement with the simple model. For instance, Figs. 12 and 13 show the locations of the fixed points on the surface of the droplet at $x=0$ and $y=0$, respectively. For the interfacial drop, the fixed points are found numerically using a bounded Newton's method, while for the submerged droplet they are obtained by solving Eq. (51). In each case, we find a pair of bifurcations as τ_{12} is increased from zero. These occur at $\tau_{12}^{ds}=4/15\approx0.27$ and $\tau_{12}^{sn}=2/\sqrt{50}\approx0.28$ in the model of the submerged droplet and at $\tau_{12}^{ds}\approx0.31$ and $\tau_{12}^{sn}\approx0.41$ for the interfacial drop.

For the submerged droplet we find a symmetric pair of fixed points in the $y=0$ plane below τ_{12}^{ds}. A degenerate saddle-

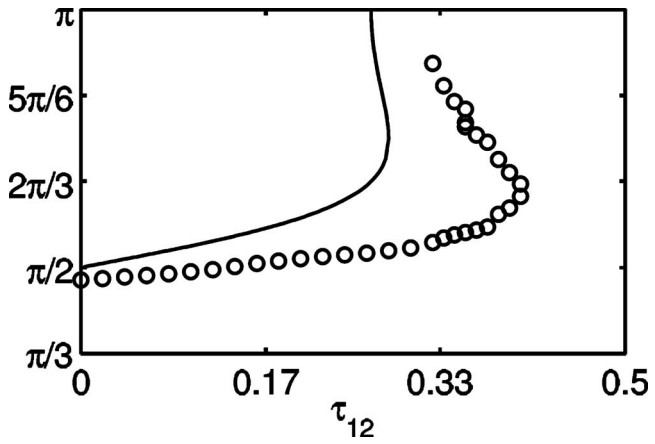

FIG. 13. The polar angle of the fixed points on the surface of the submerged (solid line) and the interfacial droplet (circles) restricted to the $y=0$ plane. The fixed points at the contact line, $\theta=\theta_c$, are not shown.

node bifurcation at τ_{12}^{ds} leads to the creation of two additional symmetric pairs of fixed points at $\theta=\pi$ (one pair in the $x=0$ plane and one in the $y=0$ plane). Another saddle-node bifurcation at τ_{12}^{sn} corresponds to the two pairs of fixed points in the $y=0$ plane colliding and disappearing. Above this value only one pair of fixed points in the $x=0$ plane remains, with the polar angle approaching $\pi/2$ for large τ_{12}.

For the interfacial drop we find exactly the same sequence of bifurcations, albeit occurring at slightly different values of τ_{12}. In addition, the interfacial droplet also possesses a pair of fixed points at the intersection of the $y=0$ plane with the contact line, in this case at $\theta_c \approx 2\pi/9$. Additional fixed points might arise near the contact line as a result of corner vortex formation at smaller values of $\theta_1+\theta_2$. The resolution of our numerical scheme, however, does not allow us to distinguish them.

Additional evidence for the qualitative similarity of the flows is found by computing the interior streamlines in the $y=0$ plane for the submerged and interfacial drop at different values of τ_{12}. These are shown in Fig. 14. In both cases, we find a pair of elliptic fixed points in the interior of the droplet (on the z axis) for $\tau_{12}<\tau_{12}^{ds}$, where the flow looks topologically similar to Hill's spherical vortex. At τ_{12}^{ds} one of the interior elliptic fixed points collides with the surface and disappears. For $\tau_{12}>\tau_{12}^{ds}$ only one fixed point is found on the z axis and the flow becomes topologically similar to rigid rotation. Similarly good qualitative agreement between the fully submerged and the interfacial droplet is found in comparing the magnitude of the velocity in the $x=0$ plane shown in Fig. 15 for different values of τ_{12}. In this and the following figures ten evenly spaced level sets of $|v_x|$ in the interval $[0, V_{max}]$ are shown, with darker shades corresponding to larger values.

Summarizing, we find the analytical model[21] based on assuming the droplet to be completely submerged in the substrate fluid to also provide a reasonably accurate representation of the flow inside interfacial droplets almost entirely submerged into the substrate fluid, with only a small cap exposed to an inviscid fluid (such as air) above. Consequently, we should expect the model to provide a reasonably accurate description of mixing inside the interfacial droplets as well, provided the assumptions on which it is based hold.

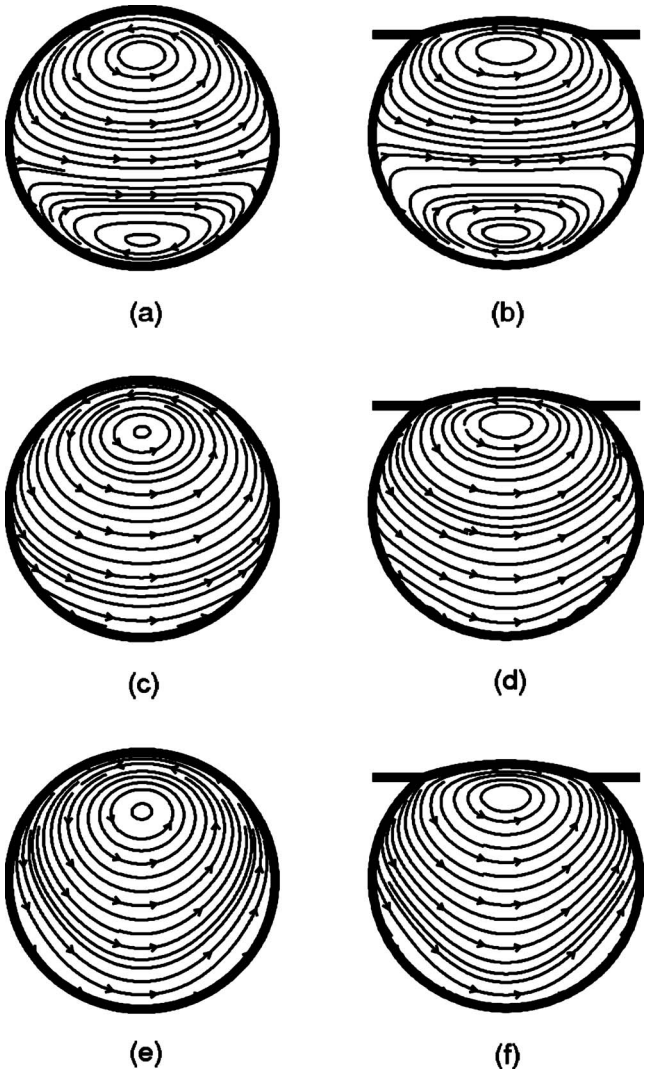

FIG. 14. Stream plots for a submerged [(a), (c), and (e)] and interfacial [(b), (d), and (f)] drop in the $y=0$ plane. Panels (a) and (b) correspond to $\tau_{12}=0.13$, (c) to $\tau_{12}=0.27$ and (d) to $\tau_{12}=0.35$, and (e) and (f) correspond to $\tau_{12}=0.50$.

2. Comparison with experiment

Next we perform a more detailed analysis of the validity of our numerical model and its predictions for the values of parameters taken from the fluid mixing experiments reported in Ref. 19. In the microfluidic device used in that study the covering fluid (fluid 1) was air. Fluorinert FC-70 was used as the substrate (fluid 2) and the droplet (fluid 3) was a water/glycerin mixture. The values of most material parameters were taken from the CRC Handbook.[34] Some parameters, such as the temperature coefficients of surface tension and the temperature gradient were estimated from indirect measurements. Other parameters (substrate thickness, and droplet radius) were measured directly. A typical setup is described by the following basic scales: $r_0=6.2\times10^{-5}$ m, $\Theta=100$ K/m, and $v_0=3.0\times10^{-5}$ m/s.

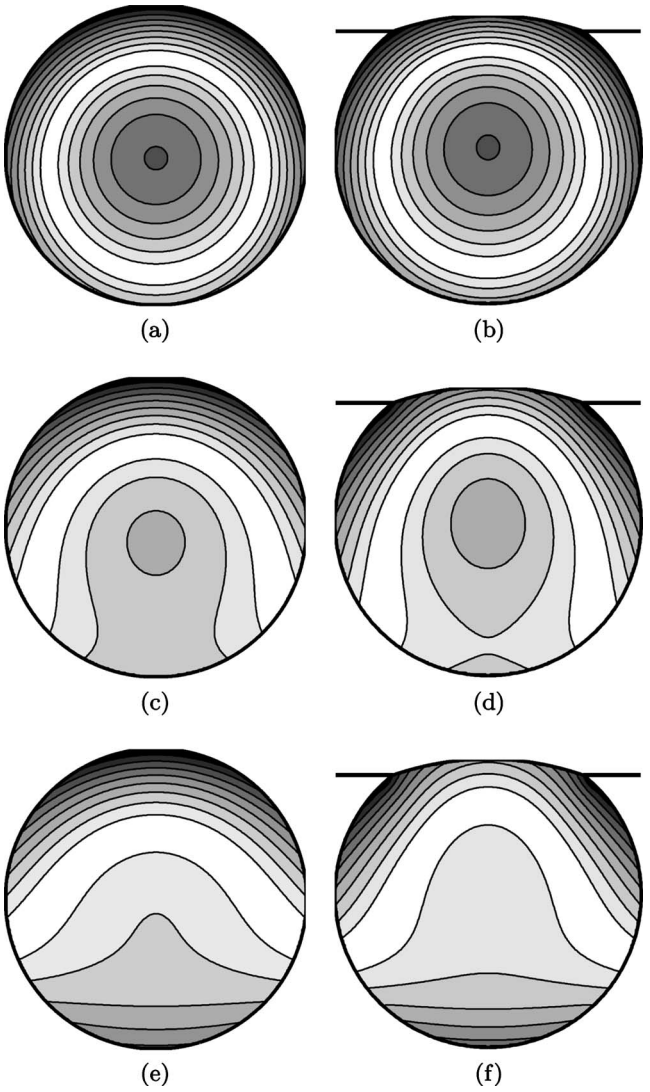

FIG. 15. The absolute value of the velocity in the $x=0$ plane for the submerged droplet [(a), (c), and (e)] and interfacial droplet [(b), (d), and (f)]. (a) $\tau_{12}=0.13$ and $V_{\max}=0.30$, (b) $\tau_{12}=0.13$ and $V_{\max}=0.29$, (c) $\tau_{12}=0.5$ and $V_{\max}=0.56$, (d) $\tau_{12}=0.5$ and $V_{\max}=0.46$, (e) $\tau_{12}=1$ and $V_{\max}=0.94$, and (f) $\tau_{12}=1$ and $V_{\max}=0.71$.

The values of the corresponding nondimensional parameters are summarized in Table III. We have not quoted the values for Re_1, Pe_1, Bo_1, and Ca_1 for the air layer due to its small values of density, viscosity, and thermal conductivity.

TABLE III. Dimensionless parameters computed from Grigoriev *et al.* (Ref. 19).

Viscosity	$\alpha_1=0.0008$	$\alpha_3=0.59$
Thermal conductivity	$\beta_1=0.036$	$\beta_3=5.9$
Surface tension	$\gamma_{12}=0.33$	$\gamma_{13}=1.2$
Temperature coefficient	$\tau_{12}=0.59$	$\tau_{13}=1.2$
Bond number	$\mathrm{Bo}_2=0.004$	$\mathrm{Bo}_3=0.0008$
Capillary number	$\mathrm{Ca}_2=1\times10^{-5}$	$\mathrm{Ca}_3=5\times10^{-7}$
Thermal Péclet number	$\mathrm{Pe}_2=35$	$\mathrm{Pe}_3=0.02$
Reynolds number	$\mathrm{Re}_2=0.096$	$\mathrm{Re}_3=2\times10^{-4}$
Length	$\lambda=4\times10^4$	$\chi=64$

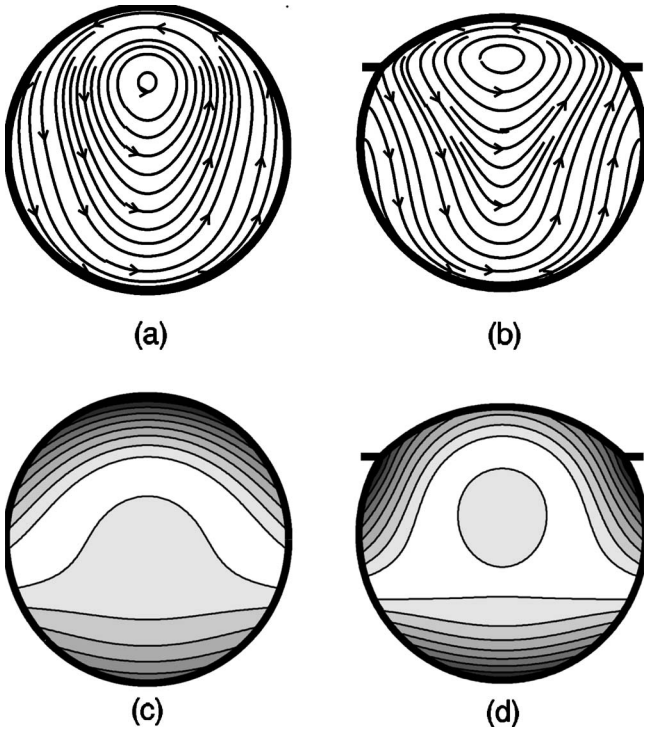

FIG. 16. The interior flow field for the light glycerin/water mixture. Shown are the streamlines for the submerged (a) and interfacial (b) droplet in the $y=0$ plane and the magnitude of v_x for the submerged (c) and interfacial (d) droplet in the $x=0$ plane. $V_{\max}=0.58$ and 0.33 in (c) and (d), respectively. The parameters are as in Table III.

The heat and momentum fluxes in air are too small to significantly affect the temperature and velocity fields inside the droplet and the substrate fluid.

A quick inspection of Table III shows that most of the nondimensional parameters have the order of magnitude assumed in Sec. II. One notable exception is the large value of the Péclet number Pe_2 in the substrate fluid. This means that at large distances from the droplet heat transport is advection—rather than diffusion—dominated and hence our asymptotic solution (12) is inaccurate for such large temperature gradients. A more accurate analysis of the asymptotic flow profile (to be presented in a subsequent publication) shows that the temperature gradient acquires a vertical component for larger values of Pe. As we discussed previously, the validity of the present numerical model can be restored by reducing the magnitude of the temperature gradient.

In the experiment, the easiest parameter to modify was α_3, the ratio of the droplet viscosity to that of the substrate. With this in mind, we have computed and compared the velocity field for different values of α_3. For intermediate values of α_3, the streamlines of the flow in the $y=0$ plane and the absolute value of v_x at $x=0$ are shown in Fig. 16. A quick comparison of the numerical solution and the simplified model flow (49) shows that the two are quite similar. In particular, the topological structure of both flows is dominated by a continuous set of elliptic fixed points in the $x=0$ plane (see Fig. 17), anchored at the z axis near the top of the droplet and extending all the way to the droplet surface (the bulk of the fluid circulates around the curved line represent-

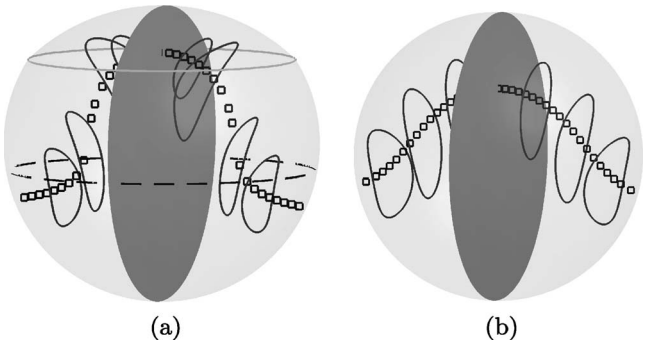

FIG. 17. Invariant sets of the flow inside (a) the interfacial droplet and (b) the fully submerged droplet. The open squares represent the set of elliptic fixed points in the $x=0$ plane. The solid lines are sample 3D steamlines and the dashed line is a heteroclinic orbit connecting the stable and unstable spiral fixed points. The surface of the droplet (light gray), the $y=0$ plane (dark gray), and the contact line are also invariant sets.

ing this set). One should, therefore, expect the model to provide a qualitatively accurate description of the flow (and hence its mixing properties) almost everywhere inside the interfacial droplet.

On the other hand, one finds that the simplified model, for the same values of parameters, does not capture some finer details of the flow near the droplet surface, such as the pairs of spiral and saddle fixed points [see Fig. 18(a)] and the heteroclinic orbits connecting the spiral fixed points (see Fig. 17). The emergence of such invariant structures can, in principle, radically alter the mixing properties of the flow, either enhance or impede mixing, near the surface (and possibly near the $y=0$ plane). In practice, however, the regions where the predictions of the model disagree with the numerics are characterized by small values of the velocity, so in either case the flow will have poor mixing properties there. To be fair, we should also mention that, for slightly different values of parameters, similar spiral flow structures arise near the droplet surface in the simplified model, as Fig. 18(b) illustrates.

The corresponding numerical solution for the flow outside the droplet is shown in Fig. 19(a). Two features of this flow are worth pointing out. First of all, for the values of parameters in Table III there are two stagnation points of the flow at the front of the droplet and two at the back (more typically one finds one stagnation point at the front and one

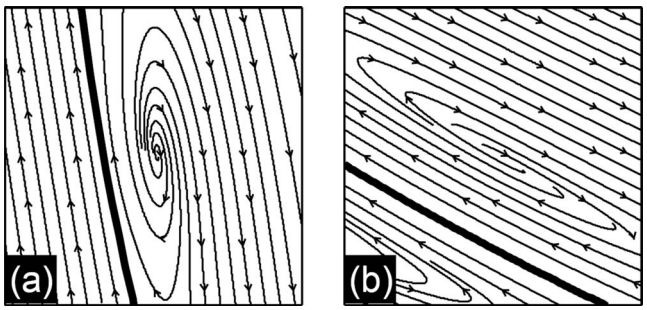

FIG. 18. Streamlines of the flow in the $y=0$ plane. (a) The blowup of Fig. 16(b) near a spiral fixed point. (b) A spiral fixed point of the flow produced by the model for $\alpha_3=0.59$ and $\tau_{13}=0.125$.

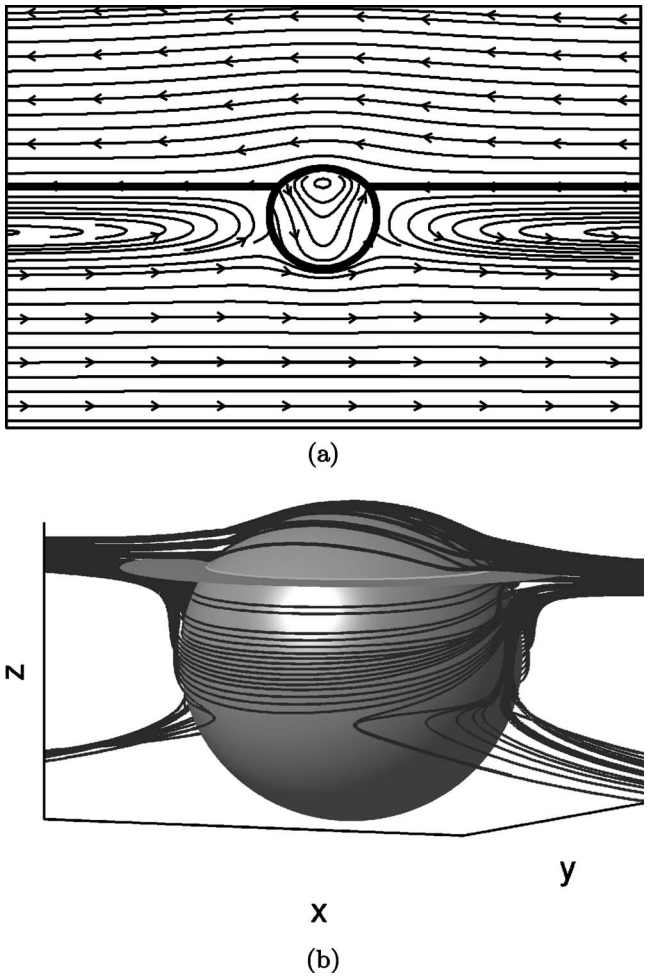

FIG. 19. The exterior flow field for the interfacial droplet with the parameters taken from Table III. Shown are 2D streamlines in the $y=0$ plane (a) and sample 3D streamlines near the droplet surface (b).

at the back). The top pair corresponds to the triple contact line, while the bottom pair corresponds to a saddle located in the vicinity of the spiral fixed point shown in Fig. 18(a) and its mirror image on the other side of the droplet. Second, the disturbance in the exterior field due to the presence of the droplet is seen to decay very quickly with the distance to the droplet, such that even near the droplet the outside flow is quite close to the asymptotic shear flow $\mathbf{V}^{\infty}$. It, therefore, should not be very surprising to find that the thermocapillary driven flow shown in Fig. 19(a) is qualitatively similar to the flow inside and around an interfacial droplet driven by external shear (compare with Fig. 6 of Ref. 24).

For a small value of the relative viscosity, $\alpha_3=0.043$, corresponding to a pure water droplet, the numerical solution and the flow predicted by model (49) are shown in Fig. 20. Again we find reasonable qualitative agreement over most of the droplet interior.

For a heavy glycerine/water mixture used in Ref. 19 the droplet is substantially more viscous than the substrate fluid, $\alpha_3=4.9$. The corresponding solutions are shown in Fig. 21. In this limit too, we find reasonable qualitative agreement between the numerical and the approximate analytical solution over most of the droplet interior. However, while the

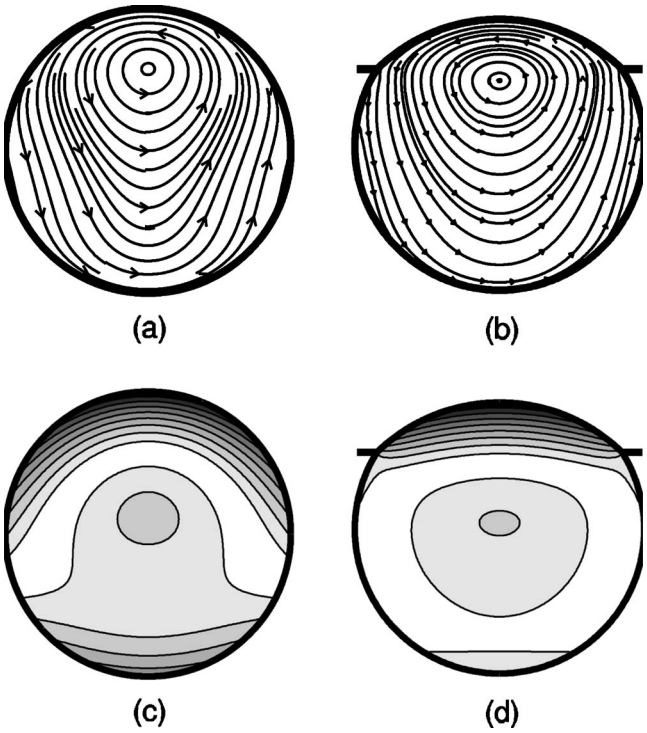

FIG. 20. The interior flow field for a pure water droplet. Shown are the streamlines for the submerged (a) and interfacial (b) droplet in the $y=0$ plane and the magnitude of v_x for the submerged (c) and interfacial (d) droplet in the $x=0$ plane. $V_{max}=0.75$ and 2.55 in (c) and (d), respectively. The parameters are as in Table III, except for $\alpha_3=0.043$.

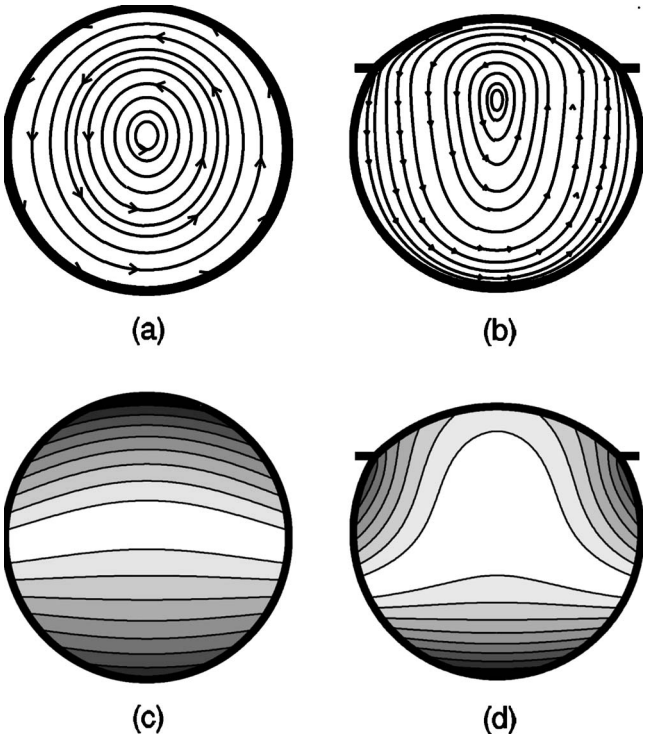

FIG. 21. The interior flow field for the heavy glycerine/water mixture. Shown are the streamlines for the submerged (a) and interfacial (b) droplet in the $y=0$ plane and the magnitude of v_x for the submerged (c) and interfacial (d) droplet in the $x=0$ plane. $V_{max}=0.37$ and 0.15 in (c) and (d), respectively. The parameters are as in Table III, except for $\alpha_3=4.9$.

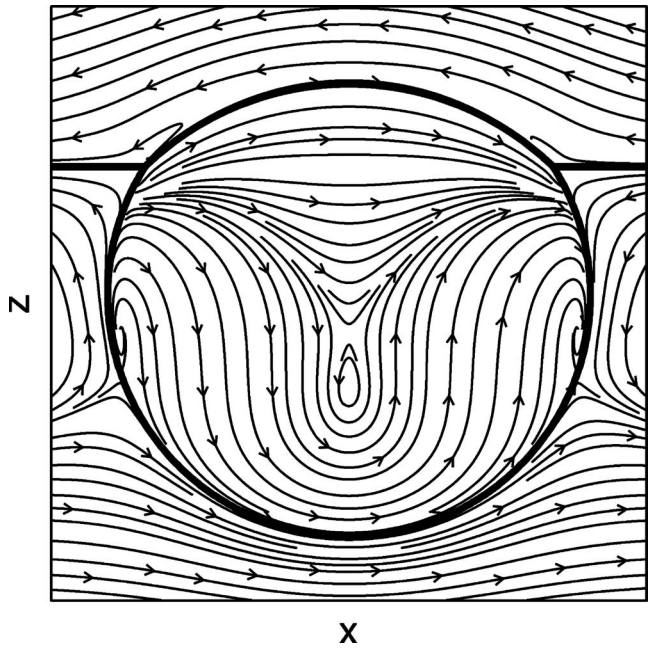

FIG. 22. Interior flow with complex topology. Shown are streamlines in the $y=0$ plane. The parameters are as in Table III, except for $\tau_{13}=6\times10^{-3}$.

model predicts the flow to be almost identical to solid rotation around the y axis (i.e., quasi-2D), the boundary conditions at the triple contact line force the numerical solution inside the interfacial droplet to retain a distinctly three-dimensional (3D) structure, as the level sets of v_x shown in Fig. 21(d) illustrate.

To conclude this section, we would like to point out that the parameter space of the problem is too large to fully explore. However, changing even just one of the parameters relative to the experimental values can produce interior flows with substantially more complex structure. One such flow is presented in Fig. 22. In contrast to the other cases considered in this section, we now find that the flow is organized around *two* sets of fixed points in the $x=0$ plane extending from the z axis to the surface of the droplet [see Fig. 23(a)]. While the bottom set is again composed of elliptic fixed points, the top

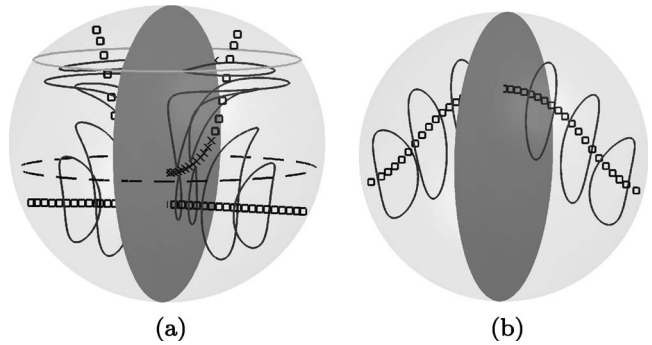

FIG. 23. Invariant structures of the flow are shown for the interfacial (a) and the submerged droplet (b). The open squares and crosses represent the sets of elliptic and saddle fixed points, respectively, in the $x=0$ plane. The solid lines are sample 3D streamlines and the dashed line is a heteroclinic orbit connecting the stable and unstable spiral points. The invariant sets contained inside the $y=0$ plane are not shown. The parameters are as in Table. III, except for $\tau_{13}=6\times10^{-3}$.

set is made up of saddles near the z axis and elliptic fixed points near the surface. The important new feature of the flow is that the spirals now affect the flow globally, so model (49) provides an adequate description of the flow *nowhere* inside the droplet.

V. CONCLUSION

To summarize, we have numerically solved the problem of thermocapillary migration of a droplet (or liquid lens) suspended at a free interface of two immiscible fluids (the substrate and the covering fluid) in response to an imposed weak horizontal temperature gradient. The numerical method used a boundary collocation scheme to compute the velocity and temperature fields in the three fluids in terms of Lamb's general solution and spherical harmonic expansions, respectively. The method was found to produce accurate (in terms of the residual) solutions for generic choices of parameters. However, the numerical solutions were found to become inaccurate, at large values of the truncation order, when the droplet was either (i) strongly stretched due to a large surface tension at the substrate's free surface or (ii) almost completely expelled by, or immersed in, the substrate. This was found to be a result of the condition number of the system of equations representing the boundary conditions on the collocation rings becoming very large, illustrating the limitations of Lamb's/spherical harmonic expansions in geometries deviating strongly from spherical.

We have computed the velocity of thermocapillary migration for interfacial droplets as a function of the eight nondimensional parameters and found the results to differ dramatically from the classical problem of thermocapillary migration in the bulk.[1] Most important, for typical values of parameters, interfacial droplets were found to migrate in the direction opposite to the temperature gradient, while in the classical problem migration is always in the direction of the gradient. For interfacial droplets, the migration speed is determined primarily by the motion of the substrate fluid caused by the thermocapillary effect at its free surface and hence is strongly dependent on the boundary conditions for the substrate layer. The thermocapillary effect on the droplet surface responsible for the motion of the droplet relative to the substrate's free surface (see Sec. IV B) provides only a relatively small correction.

This study was largely motivated by the problem of mixing inside thermocapillary driven droplets. Although qualitative agreement was found between the experimental observations[19] and the predictions of a simplified analytical model,[21] it was unclear whether the model, which assumed the droplet to be completely submerged and hence spherical, was sufficiently accurate. The results reported here confirm that, for relatively small deformations of the droplet shape from a sphere, the analytical solution provides a qualitatively accurate description of the flow in most of the droplet volume. For strongly deformed droplets numerical solutions, such as those presented in this paper, become necessary.

Finally, we should mention that in the limit of vanishing Péclet numbers the velocity field is symmetric with respect to the $x=0$ plane, so that all streamlines are closed and the flow is integrable. Mixing via chaotic advection requires this symmetry to be broken. In the analysis of Ref. 21, symmetry breaking resulted from assuming the temperature gradient to be nonuniform. In fact, for temperature boundary conditions relevant to experiments, no such assumption is necessary. For finite Péclet numbers the temperature gradient acquires a vertical component due to the advection of heat in the substrate, breaking the symmetry and making the flow nonintergrable,[35] even in the simplified model. Incorporating the effect of a vertical temperature gradient into the numerical model is currently underway; the results will be reported in a subsequent publication.

ACKNOWLEDGMENTS

We would like to thank Peter Mucha for his input in the early stages of this investigation and Michael Schatz, Vivek Sharma, and Daniel Borrero for sharing the experimental results. This material is based upon work supported by the National Science Foundation under Grant No. 0400370. Acknowledgment was also made to the donors of the American Chemical Society Petroleum Research Fund for partial support of this research.

[1] N. O. Young, J. S. Goldstein, and M. J. Block, "The motion of bubbles in a vertical temperature gradient," J. Fluid Mech. **6**, 350 (1959).
[2] K. D. Barton and R. S. Subramanian, "The migration of liquid drops in a vertical temperature gradient," J. Colloid Interface Sci. **133**, 211 (1989).
[3] H. D. Smith, D. M. Mattox, W. R. Wilcox, R. S. Subramanian, and M. Meyyappan, "Experimental observation on the thermocapillary driven motion of bubbles in a molten glass under low gravity conditions," in *Materials Processing in the Reduced Gravity Environment of Space*, Proceedings of the Materials Research Society Annual Meeting, Boston, MA, November 1981, edited by G. E. Rindone (North-Holland, New York, 1982), pp. 279–288.
[4] R. L. Thompson, K. J. DeWitt, and T. L. Labus, "Marangoni bubble motion phenomenon in zero gravity," Chem. Eng. Commun. **5**, 299 (1980).
[5] D. Neuhaus, "Bubble motions induced by a temperature gradient," Naturwiss. **73**, 348 (1986).
[6] G. Wozniak, "On the thermocapillary motion of droplets under reduced gravity," J. Colloid Interface Sci. **141**, 245 (1991).
[7] P. H. Hadland, R. Balasubramaniam, G. Wozniak, and R. S. Subramanian, "Thermocapillary migration of bubbles and drops at moderate to large marangoni number and moderate Reynolds number in reduced gravity," Exp. Fluids **26**, 240 (1999).
[8] X. Ma, R. Balasubramaniam, and R. S. Subramanian, "Numerical simulation of thermocapillary drop motion with internal circulation," Numer. Heat Transfer, Part A **35**, 291 (1999).
[9] M. Meyyappan, W. R. Wilcox, and R. S. Subramanian, "The slow axisymmetric motion of two bubbles in a thermal gradient," J. Colloid Interface Sci. **94**, 243 (1983).
[10] H. Wei and R. S. Subramanian, "Thermocapillary migration of a small chain of bubbles," Phys. Fluids A **5**, 1583 (1993).
[11] Y. Wang, R. Mauri, and A. Acrivos, "Thermocapillary migration of a bidisperse suspension of bubbles," J. Fluid Mech. **261**, 47 (1994).
[12] S. Nas, M. Muradoglu, and G. Tryggvason, "Pattern formation of drops in thermocapillary migration," Int. J. Heat Mass Transfer **49**, 2265 (2006).
[13] M. Meyyappan and R. S. Subramanian, "Thermocapillary migration of a gas bubble in an arbitrary direction with respect to a plane surface," J. Colloid Interface Sci. **115**, 206 (1987).
[14] R. M. Merritt and R. S. Subramanian, "Migration of a gas bubble normal to a plane horizontal surface in a vertical temperature gradient," J. Colloid Interface Sci. **131**, 514 (1989).
[15] K. D. Barton and R. S. Subramanian, "Thermocapillary migration of a

liquid drop normal to a plane surface," J. Colloid Interface Sci. **137**, 170 (1990).
[16]M. Loewenberg and R. H. Davis, "Near-contact, thermocapillary migration of a nonconducting, viscous drop normal to a planar interface," J. Colloid Interface Sci. **160**, 265 (1993).
[17]S. H. Chen, "Thermocapillary migration of a fluid sphere parallel to an insulated plane," Langmuir **15**, 8618 (1999).
[18]R. S. Subramanian and R. Balasubramaniam, *The Motion of Bubbles and Drops in Reduced Gravity* (Cambridge University Press, Cambridge, UK, 2001).
[19]R. O. Grigoriev, V. Sharma, and M. F. Schatz, "Optically controlled mixing in microdroplets," Lab Chip **6**, 1369 (2006).
[20]S. Rybalko, N. Magome, and K. Yoshikawa, "Forward and backward laser-guided motion of an oil droplet," Phys. Rev. E **70**, 046301 (2004).
[21]R. O. Grigoriev, "Chaotic mixing in thermocapilary-driven microdroplets," Phys. Fluids **17**, 033601 (2005).
[22]D. Vainchtein, J. Widloski, and R. O. Grigoriev, "Mixing properties of steady flow in thermocapillary driven droplets," Phys. Fluids **19**, 067102 (2007).
[23]H. Brenner, "The Stokes resistance of a slightly deformed sphere," Chem. Eng. Sci. **19**, 519 (1964).
[24]K. A. Smith, J. M. Ottino, and M. O. de la Cruz, "Dynamics of a drop at a fluid interface under shear," Phys. Rev. E **69**, 046302 (2004).
[25]F. Greco, "Second-order theory for the deformation of a Newtonian drop in a stationary flow field," Phys. Fluids **14**, 946 (2002).
[26]R. V. Craster and O. K. Matar, "On the dynamics of liquid lenses," J. Colloid Interface Sci. **303**, 503 (2006).
[27]V. G. Levich, *Physicochemical Hydrodynamics* (Prentice-Hall, Englewood Cliffs, NJ, 1962).
[28]Q. Hassonjee, P. Ganatos, and R. Pfeffer, "A strong-interaction theory for the motion of arbitrary three-dimensional clusters of spherical particles at low Reynolds number," J. Fluid Mech. **197**, 1 (1988).
[29]P. Ganatos, R. Pfeffer, and S. Weinbaum, "A numerical-solution technique for three-dimensional Stokes flows, with applications to the motion of strongly interacting spheres in a plane," J. Fluid Mech. **84**, 79 (1978).
[30]N. Sneeuw, "Global spherical harmonic analysis by least-squares and numerical quadrature methods in historical perspective," Geophys. J. Int. **118**, 707 (1994).
[31]J. L. Anderson, "Droplet interactions in thermocapillary motion," Int. J. Multiphase Flow **11**, 813 (1985).
[32]J. Hadamard, "Mouvement permanent lent d'une sphere liquide et visqueuse dans un liquide visqueux," Acad. Sci., Paris, C. R. **152**, 1735 (1911).
[33]W. Rybczynski, "Translatory motion of a fluid sphere in a viscous medium," Bull. Acad. Sci. Cracovie **1a**, 40 (1911).
[34]D. R. Lide, *CRC Handbook of Chemistry and Physics*, 79 ed. (CRC, Boca Raton, FL, 1998.
[35]M. D. Bryden and H. Brenner, "Mass-transfer enhancement via chaotic laminar flow within a droplet," J. Fluid Mech. **379**, 319 (1999).